Frontiers in Bioscience Landmark

Front. Biosci. (Landmark Ed) **2026**; 31(6): 53692
https://doi.org/10.31083/FBL53692

Original Research

An Integrated Approach Reveals the Pre-Osteoblast-Driven Metrnl Synergizes With Circadian Genes to Inhibit Osteogenesis

Wenchao Fei[1], Ke Xu[1], MingMing Xu[1], Tianyi Liu[1], Xu Han[1], Conghui Zhou[1], Wenqing Tong[1], Zelin Yue[1], Yinghua Li[2,*], Yang Hong[1,3,4,*]

[1]Department of Orthopedics, The Fifth People's Hospital of Shanghai, Fudan University, 200040 Shanghai, China
[2]Central Laboratory, The Fifth People's Hospital of Shanghai, Fudan University, 200040 Shanghai, China
[3]Shanghai Clinical Research Center for Aging and Medicine, 200040 Shanghai, China
[4]Center of Community-Based Health Research, Fudan University, 200040 Shanghai, China
*Correspondence: fdwy_liyinghua@outlook.com (Yinghua Li); sci_hongyang@sina.com (Yang Hong)
Academic Editor: Elisa Belluzzi
Submitted: 16 February 2026 Revised: 5 May 2026 Accepted: 12 May 2026 Published: 24 June 2026

Abstract

Background: Current osteoporosis (OP) therapies predominantly suppress osteoclastic bone resorption, highlighting a critical unmet need for anabolic strategies that directly stimulate bone formation. Meteorin-like (Metrnl) is a recently identified adipokine whose role in bone metabolism remains poorly defined and controversial. This study systematically investigated the expression profile, physiological function, and molecular mechanism of Metrnl in skeletal biology. **Methods**: An integrated approach combining clinical bone marrow specimen analysis, proteomics, single-cell RNA sequencing, and conditional genetic ablation mouse models was utilized. Skeletal phenotypes were evaluated via Micro-CT and bone histomorphometry. Intracellular molecular interactions were determined through co-immunoprecipitation and transcriptional activity assays. **Results**: Clinically, Metrnl expression was significantly diminished in bone marrow samples from postmenopausal women with OP, suggesting potential relevance to human disease. In mice, Metrnl was predominantly expressed in osteoprogenitor cells, and its expression declined progressively with age. Unexpectedly, systemic knockout (n = 6 per group) of Metrnl resulted in a marked increase in trabecular bone mass (bone volume to total volume ratio [BV/TV]: 4.11 ± 0.08% vs. 3.89 ± 0.12%, $p < 0.01$) and bone formation rate (Bone formation rate per bone surface [BFR/BS]: 0.50 ± 0.03 vs. 0.38 ± 0.03 μm/day*100, $p < 0.05$) without affecting osteoclast activity. This anabolic phenotype was fully recapitulated in osteoblast-specific (Ocn-Cre) and osteoprogenitor-specific (Prx1-Cre) conditional knockout mice (n = 6 per group), which both exhibited significantly higher BV/TV (4.13 ± 0.06% and 4.04 ± 0.05%, respectively) compared to controls (3.88 ± 0.08%; $p < 0.001$ and $p < 0.01$, respectively), establishing a cell-autonomous inhibitory role of Metrnl in osteogenesis. Mechanistically, intracellular Metrnl directly interacts with the scaffold protein Receptor for activated C kinase 1 (Rack1), thereby disrupting the PKC-α–Rack1 complex, reducing Brain and Muscle ARNT-Like 1 (Bmal1) phosphorylation, and facilitating its nuclear translocation. This process subsequently upregulates transcription of the circadian clock gene Cryptochrome 2 (Cry2), thereby suppressing osteoblast differentiation. **Conclusions**: Collectively, these findings identify Metrnl as a previously unrecognized negative regulator of bone formation and uncover a Rack1-PKCα-Bmal1-Cry2 signaling axis that links circadian regulation to osteogenesis. These results establish a conceptual framework for targeting Metrnl-mediated pathways in the development of anabolic therapies for OP.

Keywords: osteoporosis (OP); Metrnl; osteogenesis; Rack1-PKCα-Bmal1-Cry2 axis; therapeutic target

1. Introduction

The global demographic shift toward population aging has been accompanied by a progressive increase in the incidence of osteoporosis (OP). Current therapeutic agents for OP, such as bisphosphonates and anti-RANKL monoclonal antibodies, predominantly act by inhibiting osteoclastogenesis or suppressing osteoclastic bone resorption activity [1]. However, pharmacological interventions that directly promote bone formation remain substantially underdeveloped, with teriparatide being one of the few clinically available agents with a well-characterized osteogenic mechanism [2]. Long-term reliance on anti-resorptive therapies may adversely affect physiological bone remodeling [3]. Moreover, these agents often demonstrate limited efficacy in conditions characterized by severe bone loss or impaired osteogenic capacity, such as senile OP [4,5]. Furthermore, prolonged bisphosphonate administration has been associated with serious adverse effects, including atypical fracture nonunion and osteonecrosis of the jaw, and emerging evidence suggests potential deterioration of bone strength [6,7,8]. Consequently, the development of novel anabolic agents that promote bone formation represents an urgent unmet medical need. Key scientific challenges in the OP research include enhancing osteogenic differentiation of bone marrow mesenchymal stem cells (BMSCs), deciphering the regulatory networks governing their lineage differentiation commitment, and sustaining osteoblastic activity and survival.

Osteoblasts (OBs), which arise from preosteoblastic cells, are responsible for collagen synthesis and bone mineral secretion, thereby facilitating bone growth and remodeling. Preosteoblastic cells predominantly reside in the bone marrow and periosteum, originate from BMSCs, and mediate bone formation and repair. The differentiation of BMSCs into functionally competent osteocytes proceeds through sequential stages, during which BMSCs progressively commit to osteoprogenitor cells ($Alp^{+}Col1a1^{+}$) and subsequently differentiate into OBs ($Alp^{++}Col1a1^{++}$) [9]. Mature OBs (Ocn^{+}) secrete collagenous and mineralized bone matrix and subsequently become embedded as mature osteocytes, which gradually undergo apoptosis under various physiological and pathological stimuli [10]. Therefore, impaired BMSC differentiation reduces the commitment of preosteoblastic cells and OBs, ultimately leading to decreased bone mass [11]. Osteoblastogenesis and osteoblastic function are orchestrated by an intricate network of cytokines across diverse physiological contexts. Pro-osteogenic cytokines, including interleukin-10, interleukin-11, interleukin-18, interferon-γ, cardiotrophin-1, and oncostatin M, promote osteoblast formation and functional activity [12,13,14,15,16]. Conversely, anti-osteogenic cytokines, such as TNF-α, TNF-β, IL-1α, IL-4, IL-7, IL-12, IL-13, IL-23, IFN-α, IFN-β, leukemia inhibitory factor, and ciliary neurotrophic factor, suppress osteoblastogenesis and associated functions [17,18,19,20]. Osteoblast formation is also regulated by multiple signaling pathways, including Wnt, parathyroid hormone (PTH), bone morphogenetic protein (BMP), transforming growth factor-β (TGF-β), fibroblast growth factor (FGF), and Hedgehog signaling [10,21,22].

Meteorin-like (Metrnl) was initially identified as an adipokine with crucial cardiovascular regulatory functions and was therefore designated as Subfatin [23]. Additionally, due to its considerable amino acid sequence homology with the neurotrophic factor Meteorin, it was also termed Meteorin-like [23]. Metrnl is currently recognized as a secretory protein, as demonstrated by Jørgensen et al. [24] through overexpression of His-tagged Metrnl in HEK293F cells and its detection in the culture supernatant. Subsequent studies have detected Metrnl in various biological fluids, including blood, intestinal secretions, and synovial fluid [25,26]. With respect to its secretion mechanism, Miao et al. [27] proposed that Metrnl is primarily secreted via the signal peptide-mediated classical endoplasmic reticulum-Golgi secretion pathway [28]. Previous studies indicate that circulating Metrnl predominantly originates from vascular endothelial cells; however, the specific cellular source of Metrnl within the bone marrow osteogenic microenvironment remains unclear [29]. Current functional studies of Metrnl have primarily concentrated on cardiovascular, metabolic, and inflammation-related fields. Li et al. [29] reported that Metrnl promotes adipogenesis and alleviates insulin resistance in adipocytes through autocrine or paracrine mechanisms. Lee et al. [30] demonstrated that exercise-induced Metrnl enhances skeletal muscle glucose uptake via phosphorylation of AMP-activated protein kinase (AMPK). Reboll et al. [31] reported that Metrnl serves as a high-affinity ligand for the KIT receptor tyrosine kinase, mediating angiogenic effects in human endothelial cells through KIT-dependent signaling pathways. In a murine myocardial infarction model, Metrnl facilitated infarct repair by selectively expanding the population of KIT-expressing endothelial cells within the infarct zone.

Research on Metrnl in bone metabolism remains limited. Gong et al. [32] reported that immunohistochemical staining revealed robust Metrnl expression in hypertrophic chondrocytes and OBs lining the trabecular bone surface. Additionally, Gong et al. [32] demonstrated that Metrnl overexpression in the MG63 cell line suppressed osteogenic differentiation under osteogenic induction conditions. Subsequent studies have suggested a potential regulatory role for Metrnl in skeletal tissues. For instance, Invernizzi et al. [33] suggested that Metrnl may modulate bone-muscle crosstalk following spinal cord injury, thereby potentially influencing bone remodeling and muscle regeneration [34]. Huang et al. [35] investigated the role of Metrnl in skeletal development and fracture healing using murine models. Their findings revealed that during development, Metrnl was expressed in the perichondrium and primary ossification centers. Metrnl knockout did not alter skeletal parameters in utero, at birth, or during postnatal growth. At 6 weeks of age, Metrnl-deficient mice exhibited body length, body weight, tibial length, femoral length, bone volume/total volume (BV/TV), trabecular number, trabecular thickness, and cortical thickness comparable to those of control littermates. In 4-month-old mice, Metrnl deficiency did not modify femoral bone strength, and the authors further reported that Metrnl promoted osteoblast differentiation . These conclusions contradict the findings of Gong et al. [32], highlighting that the precise role of Metrnl in skeletal development and bone metabolism remains to be fully elucidated. Numerous key scientific questions remain unresolved, including the primary cellular source of Metrnl in bone, the target cell types through which it exerts regulatory effects, the consequences for skeletal growth and metabolism, and the underlying molecular mechanisms involved. Addressing these issues requires rigorous experimental validation using integrated cellular and *in vivo* approaches.

Therefore, in this study, we employed a multidimensional and integrative approach to systematically decode the role of Metrnl in skeletal biology. By leveraging high-throughput proteomics and single-cell RNA sequencing (scRNA-seq), we first identified the age-related decline of Metrnl and its precise enrichment within the preosteoblast population. To achieve high-resolution spatial validation, multiplex immunofluorescence labeling (TSA) was utilized to visualize the co-localization of Metrnl within

the osteogenic niche. Furthermore, through the generation of global and cell-specific conditional knockout murine models, we uncovered an unexpected cell-autonomous inhibitory role of Metrnl in bone formation. To elucidate the underlying molecular architecture, we integrated co-immunoprecipitation (Co-IP) with advanced molecular dynamics (MD) simulations and computational modeling, which collectively identified a novel Metrnl-Rack1 physical interaction. These innovative methodologies allowed us to characterize the previously unrecognized Metrnl-Rack1-PKCα-Bmal1-Cry2 signaling axis, providing a refined conceptual framework for targeting circadian-coupled pathways in the development of anabolic therapies for osteoporosis.

2. Methods

2.1 Cell Culture

MC3T3-E1 cells (Cell Bank of the Chinese Academy of Sciences, SCSP-5218) at passages 4-10 were cultured in α-minimum medium (α-MEM,12561072, Gibco, Grand Island, NY, USA) supplemented with 10% fetal bovine serum (FBS, 10099, Gibco, Grand Island, NY, USA) under standard conditions (37 °C, 5% CO_2). The cells were authenticated by STR profiling(**Supplementary Material 1**) and regular mycoplasma testing consistently yielded negative results.

2.2 Western Blot (WB)

Total proteins were extracted from cultured cells using RIPA lysis buffer (Sigma Aldrich, 20-188) supplemented with 1% phenylmethylsulfonyl fluoride (PMSF; Sigma Aldrich, 10837091001). Protein concentrations were quantified using a BCA Protein Assay Kit (Beyotime, P0012S) according to the manufacturer's protocol, and equal amounts of protein (30 μg per lane) were resolved by SDS-PAGE. Electrophoresis was performed at 90 V for approximately 20 min, followed by 120 V until the dye front reached the bottom of gel. Proteins were transferred onto polyvinylidene difluoride (PVDF) membranes using a wet transfer system at 200 mA, with transfer time adjusted according to protein molecular weight. Membranes were blocked with 5% skim milk for 2 h at room temperature (5% bovine serum albumin was used for phosphorylated proteins), and then incubated overnight at 4 °C with primary antibodies diluted in Tris-buffered saline containing 0.1% Tween-20 (TBST) according to the manufacturer's instructions with gentle agitation. After three washes with TBST (10 min each), membranes were incubated with species-specific horseradish peroxidase (HRP)-conjugated secondary antibody (1:10,000 in TBST) for 1 h at room temperature. Following three additional TBST washes, protein bands were visualized using an enhanced chemiluminescence system and images were captured with the Tanon 5200 Multi Chemiluminescent Imaging System (Tanon Science & Technology, Shanghai, China). The densitometric analysis of the bands was performed using ImageJ software (version 1.53, National Institutes of Health, Bethesda, MD, USA). The relative expression levels of target proteins were normalized to the gray value of the internal control (β-Actin). All experiments were performed with at least three independent biological replicates. Primary antibodies included anti-β-Actin (Cell Signaling Technology, 4970, 1:3000), anti-Metrnl (Abcam, ab235775, 1:1000), anti-Rack1 (Cell Signaling Technology, 5432, 1:1000), anti-HA (Cell Signaling Technology, 3724, 1:3000), anti- FLAG (Cell Signaling Technology, 14793, 1:1000), Anti-PKC-α (Cell Signaling Technology, 59754, 1:1000), anti- Bmal1 (Cell Signaling Technology, 14020, 1:1000), anti- Clock (Cell Signaling Technology, 5157, 1:1000), anti-Cry2 (sigma-Aldrich, SAB1300079, 1:1000). HRP-conjugated secondary antibodies were obtained from Boster (anti-rabbit IgG, BA1055; anti-mouse IgG, BA1050; both at 1:5000).

2.3 Quantitative Real-Time Polymerase Chain Reaction (QRT-PCR)

Total RNA was extracted from cells using TRIzol Reagent (Invitrogen, Carlsbad, CA, USA) according to the manufacturer's instructions. The purity and concentration of RNA were determined using a NanoDrop 2000 spectrophotometer (Thermo Fisher Scientific). Subsequently, 1 μg of total RNA was reverse-transcribed into complementary DNA (cDNA) using the PrimeScript™ RT Master Mix (Takara Bio, Shiga, Japan). Quantitative real-time PCR was performed on an ABI 7500 Real-Time PCR System (Applied Biosystems, CA, USA) using the TB Green® Premix Ex Taq™ II (Tli RNaseH Plus) kit (Takara Bio). The reaction mixture (20 μL) consisted of 10 μL of TB Green Premix, 0.8 μL of each forward and reverse primer (10 μM), 0.4 μL of ROX Reference Dye, 2 μL of cDNA template, and 6 μL of ddH2O. The thermal cycling conditions were as follows: initial denaturation at 95 ℃ for 30 s, followed by 40 cycles of 95 ℃ for 5 s and 60 ℃ for 34 s. GAPDH served as an internal control, and relative gene expression levels were calculated by the $2^{-\Delta\Delta CT}$ method. Primer sequences are listed in Table 1.

2.4 GST Pull-Down

Recombinant GST-HA-Metrnl (bait) or Flag-Rack1 (prey) were expressed and purified as described in Section 2.17. Approximately 5–10 μg of the GST-tagged bait protein was immobilized on pre-equilibrated glutathione-sepharose 4B beads for 2 hours at 4 ℃. After washing to remove unbound proteins, equimolar amounts of the Flag-tagged prey protein were added and incubated overnight at 4 ℃ with gentle rotation. The beads were then washed five times with pre-cooled PBST buffer to eliminate non-specific binding. Finally, the bound complexes were eluted by boiling in 1× SDS loading buffer for 10 minutes and analyzed via Western blot using anti-HA and anti-Flag antibodies to verify the direct binding.

Table 1. Primers used in qPCR.

Genes	Forward primer	Reverse primer
Gapdh	AGGTCGGTGTGAACGGATTTG	GGGGTCGTTGATGGCAACA
Ctsk	CTCGGCGTTTAATTTGGGAGA	TCGAGAGGGAGGTATTCTGAGT
Trap	CTGGAGTGCACGATGCC AGCGACA	TCCGTGCTCGGCGATGGACCAGA
V-ATPase-d2	AAGCCTTTGTTTGACGCTGT	TTCGATGCCTCTGTGAGATG
Alp	CCAACTCTTTTGTGCCAGAGA	GGCTACATTGGTGTTGAGCTTTT
Col1a1	CCCAGAGTGGAACAGCGATT	ATGAGTTCTTCGCTGGGGTG
Ocn	GAGGGCAATAAGGTAGTGA ACAGA	AAGCCATACTGGTTTGATAGCTCG
Runx2	TTCTCCAACCCACGAATGCAC	CAGGTACGTGTGGTAGTGAGT
Metrnl	TCTGTGGAGTGGATGTACCCA	CCGCACCAACAGTCTTAGTTC
Cry2	CACTGGTTCCGCAAAGGACTA	CCACGGGTCGAGGATGTAGA

2.5 Extraction of Mouse BMSCs and BMMs

Bone marrow cells were isolated from the femurs and tibias of 6-8-week-old C57BL/6 mice. Briefly, marrow was flushed with α-MEM, filtered (70 μm), and centrifuged (300 ×g, 5 min). For BMSCs, cells were cultured in α-MEM/10% FBS for 48 h, after which non-adherent cells were removed. Adherent cells were expanded for 7–10 days. For bone marrow–derived macrophages (BMMs), cells were cultured in complete α-MEM medium containing 30 ng/mL macrophage colony-stimulating factor M-CSF for 5–7 days. All primary cells, including BMSCs and BMMs, were validated for their identity by surface marker analysis using flow cytometry. The standard hierarchical gating strategy was applied to evaluate cell purity. Briefly, total events were initially gated on a forward scatter area (FSC-A) vs. side scatter area (SSC-A) plot to isolate the cell population and exclude cell debris. Single cells were subsequently selected by gating on FSC-Height (FSC-H) vs. FSC-Area (FSC-A) to exclude cell doublets. Within the single-cell gate, BMSCs were identified as $CD90^+CD105^+$double-positive cells, yielding a purity of 90% (**Supplementary Fig. 1A**). Concurrently, BMMs were identified and characterized as $CD11b^+F4/80^+$ double-positive cells, yielding a purity of 91.4% (**Supplementary Fig. 1B**).

2.6 Osteoblastic Differentiation and ALP/AR-S Staining

MC3T3 cell line or BMSCs were seeded in 24-well plates (2×10^4 cells/well) and cultured with osteogenic induction medium (α-MEM, 10% FBS, 50 μg/mL ascorbic acid, 10 mM β-glycerophosphate, 100 nM dexamethasone). After 14 days of induction, cells were fixed with 4% paraformaldehyde (PFA) and subjected to alkaline phosphatase (ALP) staining using a commercial kit (Beyotime, C3206). ALP activity was measured using ALP activity detection kits (Jiancheng Biotech, A059-2-2) and calculated according to the manufacturer's directions. For mineralization analysis, cells were stained with 2% Alizarin Red S (pH 4.2) for 30 min at room temperature. The results were obtained with an optical microscope. Subsequently, cetylpyridinium chloride monohydrate solution (Sigma-Aldrich, C0732) was added to extract the dye, and the absorbance (562 nm) was measured with a microplate reader (Infinite M200 Pro NanoQuant; Tecan Group Ltd., Männedorf, Switzerland).

2.7 Osteoclastogenesis and TRAP Staining

BMMs (3×10^4 cells/well) were cultured in 48-well plates with 30 ng/mL M-CSF (R&D Systems, #416-ML) and 50 ng/mL RANKL (R&D Systems, #462-TEC) for osteoclast induction. On day 8, cells were fixed with 4% PFA and subjected to TRAP staining (Sigma-Aldrich, 387A) according to the manufacturer's protocol. After incubation at 37 °C for 30–60 min, TRAP-positive multinucleated cells (≥3 nuclei) were counted under microscopy, with semi-quantitative analysis performed using ImageJ.

2.8 Immunofluorescence (TSA)

Bone samples were fixed in 4% PFA and decalcified in 0.5 M EDTA prepared in phosphate-buffered saline (PBS) containing 0.1% PFA. Paraffin-embedded specimens were sectioned at 4–6 μm, deparaffinized, and subjected to antigen retrieval using a commercial retrieval solution (Histova Biotechnology, BoneRetrival-M, BRM5L) at 72 °C for 4–6 h. For multiplex immunofluorescence labeling, sections were sequentially incubated with primary antibodies for 2 h, followed by polyHRP-conjugated secondary antibodies and TSA fluorescence detection (Histova Biotechnology, NECC7100). Between staining cycles, antibody complexes were gently stripped using an elution buffer (Histova Biotechnology, ABCCC30) at 37 °C for 20–30 min. This process was repeated until 2–3 targets were labeled with their respective fluorophores. Primary antibodies include anti-Bmal1 (MedChemExpress, HY-P80033, 1:200), anti-Metrnl (Abcam, ab235775, 1:200), anti-Rack1 (Abclonal, A2560, 1:100), anti-Ocn (Servicebio, GB11233, 1:500), anti-Cry2 (sigma-Aldrich, SAB1300079, 1:100), anti-PDGFRα (ABclone, A2103, 1:100), anti-Sca1 (R&D Systems, AF1226, 1:100), and anti-Prx (ZEN BIO, 250163, 1:100).

2.9 Ethical Statement

The animal experiments in this study were reviewed and approved by the Animal Welfare and Ethics Committee of the Department of Laboratory Animal Science, Fudan University (Approval No. 2023-DWYY-22JZS). The study was carried out in accordance with the ARRIVE guidelines (**Supplementary Material 2**). The ethics for human sample collection were reviewed and approved by the Ethics Committee of the Fifth People's Hospital of Shanghai (Approval No. 2022020). Detailed clinical characteristics of the study participants, as well as the specific inclusion and exclusion criteria, are provided in **Supplementary Material 3**.

2.10 Enzyme-Linked Immunosorbent Assay

Blood samples were collected from mice via retro-orbital bleeding after an overnight fast (12 h) to minimize metabolic variability. Serum was obtained by centrifugation at 3000 rpm for 15 min at 4 ℃ and stored at –80 ℃. Serum biomarkers of bone metabolism, including β-CTX and P1NP, were measured using ELISA kits (Cusabio, CSB-E12775m and CSB-E16211m). Serum Metrnl levels were measured using the mouse Metrnl ELISA kit (Cusabio, CSB-EL013718MO). For the assays, serum samples were diluted 1:5 for P1NP and β-CTX, and 1:2 for Metrnl measurements, to ensure results fell within the linear range of the standard curves. All assays were performed with six independent biological replicates per group (n = 6), with three technical replicates per sample. Procedures were conducted strictly according to the manufacturer's protocols.

2.11 Alcian Blue-Alizarin Red Staining of Fetal Mouse Skeletons

Fetal mice at embryonic day 12.5 (E12.5) to postnatal day 0 (P0) were harvested with tail snips retained for genotyping and fixed in 95% ethanol for 5 days. Following fixation, skin and visceral organs were carefully dissected away under a stereomicroscope, and specimens were dehydrated in acetone for 7 days. Skeletons were then stained in Alcian Blue-Alizarin Red solution (50 mL per embryo; 0.03% Alcian Blue 8GX and 0.005% Alizarin Red S in 95% ethanol containing 1% glacial acetic acid) for 2–3 days at room temperature with daily monitoring of staining intensity. After staining, specimens were cleared in 20% glycerol for approximately 7 days until skeletal structures were clearly visualized through transparent soft tissues, and subsequently stored long-term in 50% glycerol at 4 °C.

2.12 Donor Recruitment and Samples Storage

Bone marrow cavity supernatant samples were collected from 10 female patients who underwent femoral fracture surgery at Shanghai Fifth People's Hospital between 2022 and 2023. The cohort included five young women with normal bone mass and five elderly women diagnosed with OP. Samples were stored at –80 °C until batch analysis.

2.13 Animals

Metrnl knock-out (*Metrnl*$^{-/-}$) mice and wild-type (*Metrnl*$^{+/+}$) controls on a C57BL/6J background were generated using CRISPR/Cas9 genome editing technology in collaboration with the Cyagen Biosciences Inc. (Suzhou, China). To generate conditional Metrnl knockout mice, *Metrnl*$^{Flox/Flox}$ mice were constructed by targeting exon (F: 5′-TCTCTTTGTTGTGTACCCTTAGGA-3′ R: 5′-CCTCTGGGATGTCACAGCTTTATG-3′) with flanking loxP sites via homologous recombination. These mice were crossed with Ocn-Cre (osteoblast-specific), Ctsk-Cre (osteoclast-specific), or Prx1-Cre (osteoprogenitor-specific) transgenic lines to achieve cell-type-specific Metrnl deletion. *Metrnl*$^{Flox/Flox}$Cre+ offspring served as conditional knockouts, while *Metrnl*$^{Flox/Flox}$Cre- littermates were used as controls. Genotypes were confirmed by PCR analysis of tail DNA using primers specific for loxP sites and Cre recombinase. For group allocation, a strict method of randomization was applied; mice were randomly assigned to their respective experimental groups using a computer-generated random number table. Potential confounders, such as cage location, baseline body weight, and the sequential order of Micro-CT or mechanical testing measurements, were rigorously minimized by balancing littermates across cages and processing all skeletal tissue samples in a randomized sequence. To ensure data integrity, specific inclusion and exclusion criteria were established a priori: only healthy mice with verified genotypes reaching the targeted milestones (8 weeks or 24 months of age) were included in the final analysis, while any animals exhibiting unintended severe systemic infections or non-experimental premature death were excluded. In practice, no animals or data points were excluded from the final statistical analysis. For all surgical interventions and dynamic bone labeling, mice were anesthetized via intraperitoneal injection of pentobarbital sodium (50 mg/kg). Animals were monitored daily for welfare, and humane endpoints were pre-established based on persistent weight loss or abnormal grooming behavior; at the experimental conclusion, euthanasia was performed via carbon dioxide (CO_2) inhalation followed by cervical dislocation. The core sample size (n = 6 per group) was determined a priori based on estimated effect sizes from our previous bone metabolism pilot studies and a statistical power analysis (power = 0.80, α = 0.05) to guarantee adequate sensitivity for detecting significant differences in the primary outcome measure, trabecular bone volume fraction (BV/TV). The specific pathogen-free facility with a 12 h light/dark cycle and controlled temperature and humidity was used to house mice. All procedures were approved by the Institutional Animal Care and Use Committee of Fudan University.

2.14 Micro-CT Analysis

Femurs were immersed in 75% ethanol at 4 °C and scanned with a Bruker Skyscan 1176 micro-CT system

(Bruker, Kontich, Belgium). The scanning parameters were set as follows: X-ray source voltage of 50 kV, source current of 180 µA, and a 0.5 mm aluminum filter for beam hardening reduction. Images were acquired with an exposure time of 950 ms, a rotation step of 0.400° over a 180° rotation, and a frame averaging of 2. The image pixel size (voxel resolution) was 6.48 µm using 2 × 2 camera binning. The raw projection data were reconstructed using NRecon software (version 1.7.4, Bruker microCT, Kontich, Antwerp, Belgium) based on the Feldkamp algorithm, with a beam hardening correction of 33%, a ring artifact correction of 6, and a smoothing level of 1. DataViewer software (Bruker) was used for image pre-processing. The region of interest (ROI) was defined as the area starting 0.5 mm distal to the growth plate and extending for 100 slices. For bone segmentation, a global thresholding method was applied in CTAn software (Bruker) to distinguish mineralized bone from soft tissue and calculate structural indices. 3D reconstructions were performed using CTvox software (Bruker). Parameters analyzed included bone mineral density (BMD), bone volume to total volume ratio (BV/TV), bone surface-to-volume ratio (BS/TV), trabecular number (Tb.N), trabecular separation (Tb.Sp), trabecular thickness (Tb.Th), and trabecular pattern factor (Tb.pf). Investigators performing micro-CT were blinded to the genotypes and group allocations using double-blinded sample coding.

2.15 Bone Histology and Histomorphometry

For dynamic histomorphometric analysis, calcein green (15 $mg \cdot kg^{-1}$ body weight) was injected intraperitoneally into 12-week-old *Metrnl*$^{+/+}$ and Metrnl$^{-/-}$ mice, followed by a second injection 7 days later. Mice were sacrificed at 14 weeks of age. After fixation in 10% formaldehyde for 3 days, undecalcified femurs were dehydrated in increasing concentrations of ethanol, cleared in xylene and embedded in methyl methacrylate (MMA). Mineral apposition rate (MAR) was analyzed for each sample using BIOQUANT OSTEO Image Analysis Software (version 2022, BIOQUANT Image Analysis Corporation, Nashville, TN, USA). Static histomorphometric parameters of bone volume over total bone (BV/TV), osteoclast number (OC.N/BS), and osteoclast surface per bone surface (OC.S/BS) were acquired from PFA-fixed, paraffin-embedded, decalcified bone sections stained with H&E or TRAP. Histological images were captured using an Eclipse TS100 light microscope (Nikon Corporation, Japan) and analyzed using ImageJ software (NIH, Bethesda, MD, USA). Investigators performing histological measurements were blinded to the genotypes and group allocations using double-blinded sample coding.

2.16 Single-Cell Bioinformatics Analysis

To systematically map the expression profile of Metrnl within the bone marrow microenvironment, we performed a targeted search of the NCBI Gene Expression Omnibus (GEO) database. The GSE132151 dataset was specifically selected based on the following criteria: (1) it provides high-resolution single-cell transcriptomic profiling of the non-hematopoietic cell compartment in mouse bone marrow; (2) it comprehensively captures the continuous differentiation spectrum of the osteogenic lineage, ranging from mesenchymal stem cells (BMSCs) to mature osteoblasts; and (3) it includes well-defined clusters of adipogenic progenitors, allowing for the assessment of Metrnl in the context of bone-fat lineage commitment. Data from 5107 cells were normalized and subjected to graph-based clustering using the Louvain algorithm. The top 20 principal components (PCA) and 2000 highly variable genes were used for downstream analysis. Cells were clustered into five populations (BMSC, osteoblast progenitor, pre-osteoblast, adipocyte progenitor, pre-adipocyte) via UMAP, and Metrnl expression across clusters was visualized using violin plots.

2.17 Plasmid Construction and Recombinant Protein Production

2.17.1 Plasmids for Mammalian Cell Expression and Lentivirus Production

The helper plasmids for lentiviral production included psPAX2 and pVSVG. The transfer vectors used were pLKO.1-puro, pLKO.1-hygro, PCDH-puro, PCDH-hygro, and PCDH-neo. For gene knockdown, three short hairpin RNAs (shRNAs) targeting mouse *Metrnl* were commercially synthesized and cloned into the *Age*I/*Eco*RI sites of the pLKO.1-puro vector: Sh1: 5′-CCGGCACGCTTTAG TGACTTTCAAACTCGAGTTTGAAAGTCACTAAAG CGTGTTTTTTG-3′ Sh2: 5′-CCGGGCTTCCAGTATGA GCTGATGACTCGAGTCATCAGCTCATACTGGAAG CTTTTTTG-3′ Sh3: 5′-CCGGGCTTCCAGTATGAGCT GATGACTCGAGTCATCAGCTCATACTGGAAGCTT TTTG-3′.

For overexpression, the full-length coding sequences (CDS) of mouse *Metrnl*, *Rack1*, and *Cry2* were amplified using PrimeSTAR® Max DNA Polymerase (Takara) and inserted into the PCDH series vectors via *Eco*RI/*BamH*I sites. All constructs were verified by Sanger sequencing.

2.17.2 Plasmids for Prokaryotic Protein Expression

To generate recombinant proteins for GST pull-down assays, the mouse Metrnl CDS (with an HA tag) was cloned into the pGEX-4T-1 vector to produce the GST-HA-Metrnl bait. The Rack1 CDS (with a Flag tag) was cloned into the pET-28a vector to produce the Flag-Rack1 prey.

2.17.3 Recombinant Protein Expression and Purification

The recombinant plasmids were transformed into Escherichia coli BL21 (DE3). Cultures were grown in LB medium containing 100 µg/mL ampicillin or 50 µg/mL kanamycin at 37 °C with shaking at 220 rpm until the OD_{600} reached 0.6–0.8. Protein expression was induced with 0.5

mM IPTG at 16 °C for 16 h. Cells were harvested by centrifugation (5000 ×g, 15 min, 4 °C) and resuspended in Lysis Buffer (ice-cold PBS, 1% Triton X-100, 1 mM PMSF, and protease inhibitor cocktail). The suspension was lysed via sonication (work 3 s, stop 5 s, power 200 W, total 15 min) and cleared by centrifugation (12,000 ×g, 30 min, 4 °C).

For purification: GST-HA-Metrnl: The supernatant was incubated with Glutathione Sepharose 4B beads (GE Healthcare) at 4 °C for 2 h. Bound proteins were washed five times with PBST and eluted with Elution Buffer (50 mM Tris-HCl, pH 8.0, containing 20 mM reduced glutathione). Flag-Rack1: The supernatant was incubated with Anti-FLAG® M2 Affinity Gel (Sigma-Aldrich) at 4 °C for 4 h. Bound proteins were eluted with 3×Flag peptide (150 μg/mL).

Protein concentration was determined using a BCA Kit (Beyotime). The quality and purity were validated by 10% SDS-PAGE followed by Coomassie Brilliant Blue staining.

2.18 Mechanical Testing

The femur was subjected to a three-point bending test using an Instron 5967 universal testing machine (Instron Corp, 5967). After applying a preload of 0.01 N, continuous loading was performed at a rate of 1 mm/min until fracture, and the maximum load was measured.

2.19 Co-Immunoprecipitation (IP)

For *in vitro* co-immunoprecipitation (co-IP) assays, HA- or FLAG-tagged proteins were produced in HEK293T cells (Cell Bank of the Chinese Academy of Sciences, SCSP-502) transfected by Lipofectamine 2000 with corresponding plasmids. For *in vivo* co-IP, BMSCs were isolated and cultured from wild-type (WT) mice. Total cell lysates were incubated overnight at 4 °C with antibodies or normal IgG (Santa Cruz Biotechnology Inc., sc-2027) as a control. Antibody-antigen complexes were precleared with Protein A/G PLUS-Agarose (Santa Cruz Biotechnology Inc., sc-2003). After several washes, samples were boiled and analyzed by immunoblot.

2.20 Computational Modeling and Molecular Dynamics Simulation

The 3D structures of Metrnl□PKC-α and Rack1 were retrieved from the AlphaFold Protein Structure Database. Protein-protein docking was performed using the ZDOCK (Fast Fourier Transform-based protein docking) algorithm to predict the potential binding modes. The top-ranked poses were evaluated based on their ZDOCK scores and biological relevance. To further analyze the 2D interaction patterns (including hydrogen bonds and hydrophobic interactions) at the Metrnl-Rack1 interface, the Ligplot (version 2.2, University College London, London, UK) software was employed. The final complex structure was visualized and pre-processed using PyMOL (v2.5) for subsequent simulations. MD simulations were conducted using the Gromacs 2022.04 package with the Amber14sb force field. The complex was centered in a cubic box with a minimum distance of 1.0 nm from the box edges and solvated with the TIP3P water model. To mimic physiological conditions, Na^+ and Cl^- ions were added to neutralize the system and achieve a final salt concentration of 0.15 M. The system underwent energy minimization using the steepest descent algorithm. For equilibration, the system was subjected to a temperature gradient from 300 K to 325 K. Subsequently, NVT (canonical) and NPT (isothermal-isobaric) ensemble equilibrations were performed for 500 ps each. Finally, a 100 ns production MD run was executed at a constant temperature (310 K or as specified) and 1 bar pressure. The integration time step was set to 2 fs, and long-range electrostatic interactions were treated using the Particle Mesh Ewald (PME) method. To quantify the binding affinity between Metrnl, PKC-α and Rack1, the binding free energy ($\Delta G_{binding}$) was calculated using the MM/PBSA (Molecular Mechanics Poisson-Boltzmann Surface Area) method via the gmx-mmpbsa tool. A total of 100–500 snapshots were extracted from the stable production trajectory (last 20 ns). The total binding free energy was calculated as the sum of the gas-phase molecular mechanical energy (Δ_{EMM}) and the solvation free energy (ΔG_{solv}): $\Delta G_{binding} = \Delta_{EMM} + \Delta G_{solv} - T\Delta S$, where Δ_{EMM} includes electrostatic and van der Waals interactions, and ΔG_{solv} comprises polar and non-polar solvation components. Trajectory analysis, including RMSD, RMSF, and Hydrogen Bond (HBOND) counts, was performed using GROMACS built-in tools. Structural snapshots and molecular animations were generated using PyMOL and VMD (Visual Molecular Dynamics). All statistical plots and data visualizations were prepared using GraphPad Prism 8.0.2.

2.21 Proteomic Analysis of Bone Marrow Cytokines

To identify differentially expressed cytokines associated with osteoporosis, bone marrow supernatant samples from 5 young women and 5 elderly women with OP were subjected to tandem mass tag (TMT)-based quantitative proteomic analysis. Briefly, proteins were extracted and quantified using a BCA Protein Assay Kit (Beyotime). Samples (100 μg each) were reduced with 10 mM DTT, alkylated with 50 mM IAA, and digested overnight with trypsin (Promega). The resulting peptides were labeled using TMTpro 16plex Reagent Kits (Thermo Fisher Scientific) and fractionated by high-pH reverse-phase HPLC. Fractions were analyzed by liquid chromatography-tandem mass spectrometry (LC-MS/MS) using a Q Exactive HF-X mass spectrometer coupled to an EASY-nLC 1200 system (Thermo Fisher Scientific). Raw data were processed using Proteome Discoverer software (version 2.4). The proteomic analysis and mass spectrometry services were performed with the assistance of APTBio (Shanghai, China).

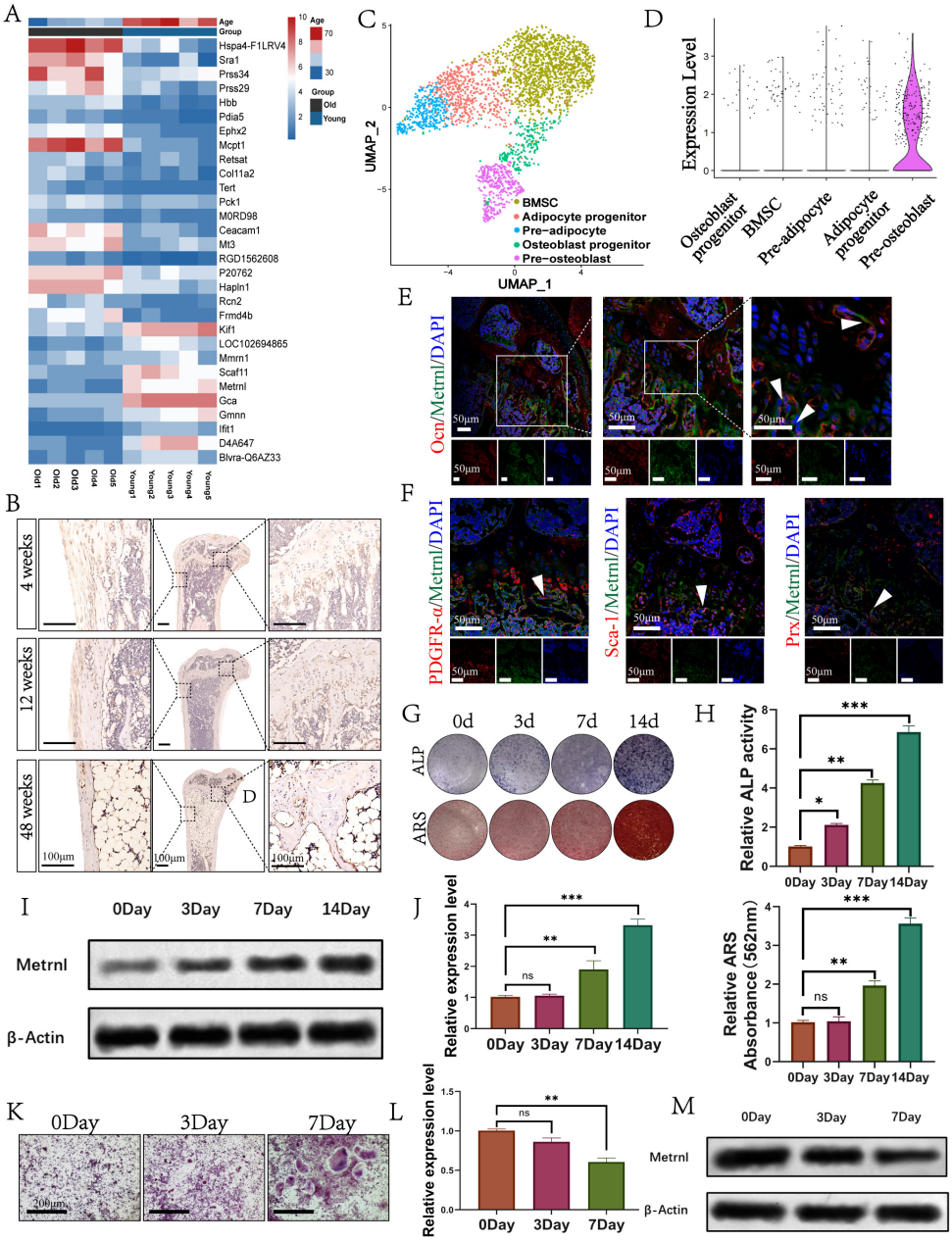

Fig. 1. Expression profile of Metrnl in bone and its expression changes during osteogenic and osteoclastic differentiation. (A) Heatmap displaying differentially expressed genes in bone marrow cytokines from 5 young women without osteoporosis and 5 elderly women with osteoporosis (OP). (B) Immunohistochemical (IHC) detection of Metrnl expression in the tibiae of mice at different ages (4, 12, and 48 weeks). Scale bar: 100 μm. (C) Single-cell RNA sequencing (scRNA-seq) analysis showing clustering of non-hematopoietic cell populations in the bone marrow. (D) Violin plots illustrating Metrnl expression levels across different cell sub-populations. (E) Immunofluorescence (IF) staining showing the co-localization of Metrnl with the osteoblast marker Ocn. Arrows indicate Metrnl+/Ocn+ cells. Scale bar: 50 μm. (F) Immunofluorescence staining showing the co-localization of Metrnl with osteoblast precursor markers Platelet-derived growth factor receptor alpha (PDGFRα), Stem cells antigen-1 (Sca-1), and Paired related homeobox 1 (Prx1). Arrows indicate Metrnl+ cells. Scale bar: 50 μm. (G) *In vitro* osteogenic differentiation assays assessed by Alkaline Phosphatase (ALP) and Alizarin Red S (ARS) staining. (H) Quantitative analysis of ALP activity and ARS absorbance during osteogenic induction. (I,J) Western blot and qPCR detection of Metrnl protein and mRNA expression levels during osteogenic differentiation. (K) *In vitro* osteoclastic differentiation assay assessed by Tartrate-resistant acid phosphatase (TRAP) staining. Scale bar: 200 μm. (L,M) Western blot and qPCR examination of Metrnl expression changes during osteoclast differentiation. Statistical significance: $*p < 0.05$, $**p < 0.01$, $***p < 0.001$, "ns" indicates no statistical significance ($p > 0.05$). Error bars represent the mean ± Standard Deviation (SD), n = 6 per group.

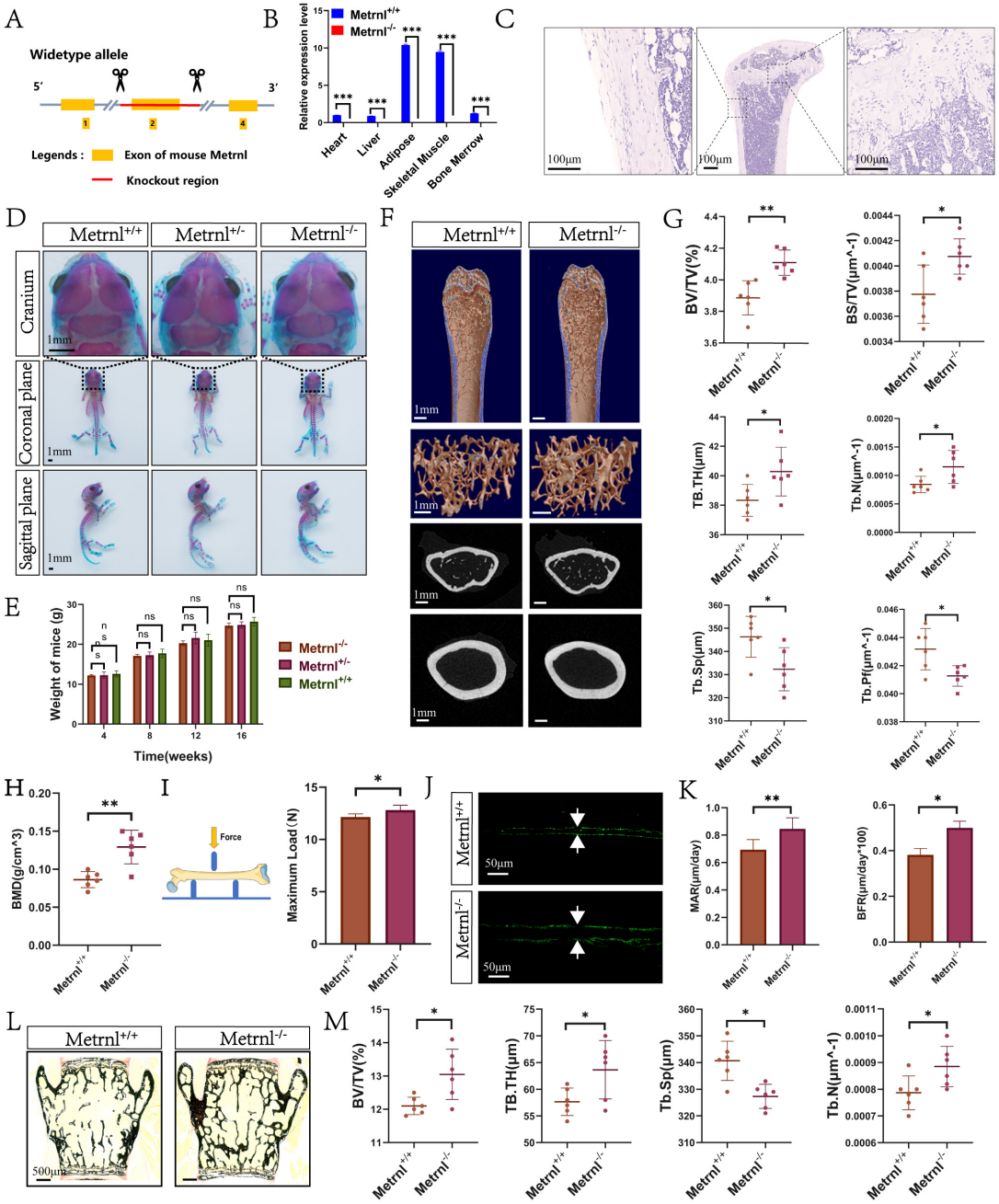

Fig. 2. Changes in bone mass and mechanical properties in global *Metrnl* knockout mice. (A) Schematic of the *Metrnl* knockout strategy via CRISPR-Cas9 technology. (B) qRT-PCR validation of *Metrnl* expression in various tissues of *Metrnl*$^{-/-}$ mice. (C) IHC staining confirming the absence of Metrnl in the bone tissue of *Metrnl*$^{-/-}$ mice. Scale bar: 100 μm. (D) Alcian Blue-Alizarin Red staining showing the whole-mount skeletons of *Metrnl*$^{-/-}$ mice and *Metrnl*$^{+/+}$ mice. Scale bar: 1mm. (E) Body weight measurements of mice from 4 to 16 weeks of age. (F) Micro-CT scans showing 3D reconstructions of the distal femur, trabecular bone, femoral cross-sections, and mid-diaphysis cortical bone. Scale bar: 1 mm. (G) Bone morphometric parameters, including BV/TV, BS/TV, Tb.Th, Tb. N, Tb.Sp, and Tb. Pf. (H) Bone Mineral Density (BMD) measurements for *Metrnl*$^{-/-}$ mice and *Metrnl*$^{+/+}$ mice. (I) Three-point bending test results for *Metrnl*$^{-/-}$ mice and *Metrnl*$^{+/+}$ mice. (J) Calcein double labeling experiment. Scale bar: 50 μm. (K) Quantitative analysis of Mineral Apposition Rate (MAR) and Bone Formation Rate (BFR/BS) in *Metrnl*$^{-/-}$ mice and *Metrnl*$^{+/+}$ mice. (L) Von Kossa staining of the fourth lumbar (L4) vertebrae. Scale bar: 500 μm. (M) Bone mass parameter analysis of Von Kossa-stained L4 vertebrae, including BV/TV, Tb.Th, Tb. N, and Tb. Sp. Statistical significance: *$p < 0.05$, **$p < 0.01$, ***$p < 0.001$, "ns" indicates no statistical significance ($p > 0.05$). Error bars represent the mean ± SD, n = 6 per group.

2.22 Data Analysis

All statistical analyses were performed using GraphPad Prism 8.0.2. The Shapiro-Wilk test was used to verify the normality of data distribution, and Levene's test was employed to assess the equality of variances. Quantitative data are presented as the mean ± standard deviation (SD). Comparisons between two groups were conducted using Student's *t*-test, while one-way or two-way analysis of variance (ANOVA) followed by Tukey's post hoc test was applied for comparisons among multiple groups. Statistical significance levels are represented as $*p < 0.05$, $**p < 0.01$, and $***p < 0.001$.

3. Results

3.1 Metrnl Is Highly Expressed in Osteoblast Precursors and Closely Associated With Osteogenic Differentiation and OP

To identify molecules potentially involved in OP, we performed proteomic profiling of bone marrow cytokines from 5 young women and 5 elderly women with OP. Thirty differentially expressed factors were identified, among which Metrnl significantly declined in the osteoporotic group, indicating a potential association with OP pathogenesis (Fig. 1A). To characterize its expression in bone tissue, we examined C57BL/6 female mice at 4, 12, and 48 weeks, representing juvenile, adult, and aged stages. High Metrnl expression was observed in the bones of 4- and 12-week-old mice (higher at 12 weeks), predominantly localized to hypertrophic chondrocytes in the growth plate, trabecular bone surfaces, and periosteum—anatomical regions enriched in osteogenic cells. In contrast, 48-week-old mice exhibited markedly reduced Metrnl expression, with only residual signal at the junction between hypertrophic zone and trabecular bone, and negligible periosteal staining (Fig. 1B). This age-dependent decline coincided with reduced osteogenic cell abundance in aged mice.

To confirm Metrnl expression in the osteogenic lineage, we performed multicolor immunohistochemistry (TSA). Ocn+ cells are used as markers of OBs. Metrnl showed substantial co-localization with Ocn, particularly in nascent trabecular bone beneath the hypertrophic zone where abundant OBs reside, indicating high Metrnl expression on trabecular surfaces (Fig. 1E). These data indicate abundant Metrnl expression in osteogenic cells and its close association with osteogenic differentiation.

To examine Metrnl expression in the osteogenic microenvironment, we analyzed dataset GSE132151. Bone marrow cells were clustered into five major populations: bone mesenchymal stem cells (BMSC), osteoblast progenitors, pre-OBs, adipocyte progenitors, and pre-adipocytes (Fig. 1C). Metrnl expression was highest in pre-OBs (Fig. 1D). Multicolor immunohistochemistry further demonstrated co-localization of Metrnl with osteoblast precursors (PDGFRα+Sca1+Prx+) (Fig. 1F). Primary bone marrow-derived mesenchymal stem cells (BMSCs) were subjected to osteogenic induction, confirmed by ALP activity and Alizarin Red absorbance (Fig. 1G,H). Both Metrnl mRNA and protein levels progressively increased during osteogenic induction (Fig. 1I,J). Conversely, in primary bone marrow macrophages (BMMs) undergoing osteoclast induction (Fig. 1K), Metrnl expression declined at both transcriptional and translational levels (Fig. 1L,M). Collectively, these results demonstrate that Metrnl is associated with OP and is preferentially expressed in osteoblast precursor populations during osteogenic differentiation.

3.2 Global Metrnl Knockout Increases Bone Mass

Global *Metrnl* knockout mice were generated using the CRISPR-Cas9 system (Fig. 2A). qRT-PCR and immunohistochemistry confirmed the absence of *Metrnl* expression in the evaluated tissues, including the heart, liver, adipose tissue, skeletal muscle, and bone marrow (Fig. 2B,C), including bone. Alcian blue-Alizarin red staining of neonatal mice showed earlier posterior fontanelle closure in *Metrnl*$^{-/-}$ mice, with no differences in skeletal size or length (Fig. 2D). Body weight was comparable between genotypes from 4 to 16 weeks (Fig. 2E), indicating no apparent differences in embryonic skeletal development or postnatal weight gain.

Micro-CT analysis of 12-week-old female femurs showed significantly increased trabecular bone mass in *Metrnl*$^{-/-}$ mice, with elevated trabecular number and thickness, while cortical bone remained unaffected (Fig. 2F). Histomorphometric analysis revealed increased bone volume/tissue volume (BV/TV), bone surface/tissue volume (BS/TV), trabecular thickness (Tb.Th), and trabecular number (Tb.N), along with reduced trabecular separation (Tb.Sp) and trabecular pattern factor (Tb.Pf) (Fig. 2G). BMD was significantly higher in *Metrnl*$^{-/-}$ mice (Fig. 2H). Three-point bending tests demonstrated enhanced maximum load-bearing capacity (Fig. 2I), indicating improved biomechanical properties. Calcein double labeling revealed increased mineral apposition rate (MAR) and bone formation rate (BFR/BS) (Fig. 2J,K). Von Kossa staining of L4 vertebrae showed consistent changes in mineralized trabeculae (Fig. 2L,M). These data demonstrate that *Metrnl* deficiency is associated with increased trabecular bone mass and elevated bone formation parameters.

3.3 Enhanced Osteogenic Differentiation in Global Metrnl Knockout Mice

To elucidate mechanisms underlying the bone phenotype, we examined osteogenic and osteoclastic differentiation *in vivo* and *in vitro*. Ocn immunostaining of tibial sections from 12-week-old females showed increased Ocn+ area and cell numbers in *Metrnl*$^{-/-}$ mice, whereas TRAP staining showed no significant change in TRAP+ signals (Fig. 3A). Osteoblast number/bone perimeter (N.Ob/B.Pm) and osteoblast surface/bone surface (Ob.S/BS) were significantly elevated, while osteoclast parameters (N.Oc/B.Pm

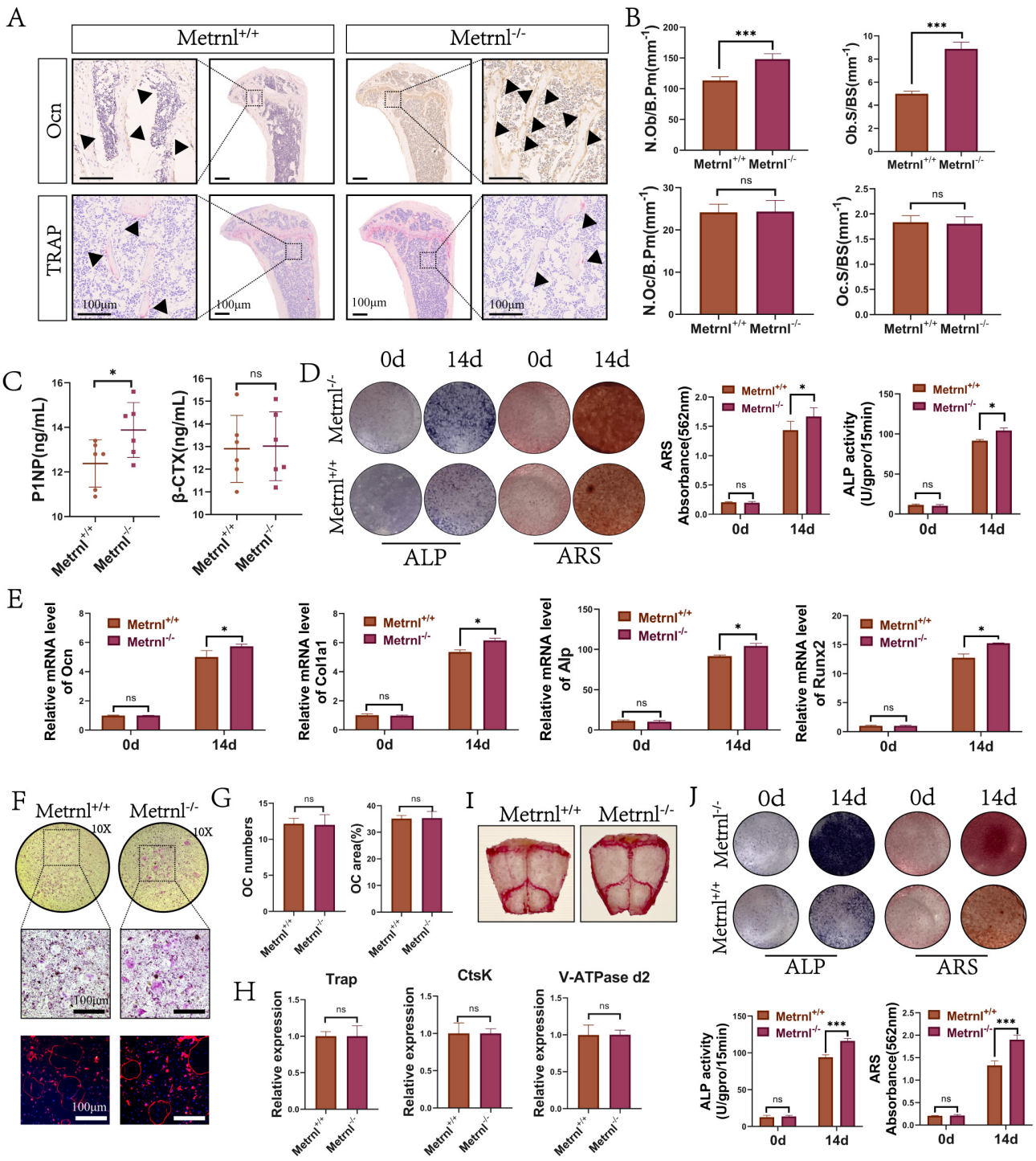

Fig. 3. Effects of global *Metrnl* knockout on osteogenic and osteoclastic differentiation. (A) Ocn IHC and TRAP staining of tibial sections from 12-week-old female mice. Arrows indicate Ocn+ or TRAP+ cells. Scale bar: 100 μm. (B) Histological parameter analysis for Ocn and TRAP staining, including N.Ob/B.Pm, Ob.S/BS, N.Oc/B.Pm, and Oc.S/BS. (C) ELISA detection of serum bone metabolism markers P1NP and β-CTX. (D) ALP and ARS staining of *in vitro* BMSC osteogenic induction at Day 0 and Day 14. (E) qRT-PCR analysis of osteogenic marker mRNA levels at Day 0 and Day 14. (F) TRAP staining and F-actin ring staining of *in vitro* BMM osteoclast induction. Scale bar: 100 μm. (G) Analysis of osteoclast number (OC.number) and area (OC.area). (H) qRT-PCR analysis of osteoclast differentiation marker mRNA levels. (I) TRAP staining of calvarial bone from 6-week-old mice. (J) ALP and ARS staining of calvarial osteoblasts at Day 0 and Day 14. Statistical Significance: *$p < 0.05$, ***$p < 0.001$, "ns" indicates no statistical significance ($p > 0.05$). Error bars represent the mean ± SD, n = 6 per group.

and Oc.S/BS) remained unchanged (Fig. 3B). Serum bone metabolism markers showed elevated P1NP in *Metrnl*$^{-/-}$ mice with no difference in β-CTX (Fig. 3C), confirming enhanced bone formation. *In vitro*, BMSCs from 4-week-old mice exhibited stronger osteogenic capacity upon Metrnl knockout, as evidenced by intensified ALP and Alizarin Red staining (Fig. 3D). mRNA levels of osteogenic markers at day 14 corroborated these findings (Fig. 3E). Osteoclast differentiation from BMMs showed no genotypic differences in TRAP staining, F-actin rings, cell number, or area (Fig. 3F,G), and mRNA expression levels of osteoclast markers were comparable (Fig. 3H). Because calvarial bones develop via intramembranous ossification, calvarial osteoclasts and OBs were further examined. TRAP staining revealed no difference in osteoclast numbers (Fig. 3I). Calvarial OBs isolated by collagenase digestion showed enhanced mineralization in *Metrnl*$^{-/-}$ mice (Fig. 3J). These results demonstrate that *Metrnl* deficiency is associated with enhanced osteogenic differentiation without detected changes in osteoclastogenesis.

3.4 Osteoblast-Specific Metrnl Deletion Increases Bone Mass

To assess the cell-specific contribution of *Metrnl*, we generated *Metrnl*$^{Flox/Flox}$ mice and crossed them with *Ocn-Cre*, *Ctsk-Cre*, or *Prx1-Cre* drivers to achieve cell-specific deletion (Fig. 4A). Micro-CT reconstruction revealed increased bone mass and trabecular number in *Metrnl*$^{Flox/Flox}$*Ocn*^{Cre} and *Metrnl*$^{Flox/Flox}$*Prx1*^{Cre} mice, but not in *Metrnl*$^{Flox/Flox}$*Ctsk*^{Cre} mice (Fig. 4B,C). Serum P1NP was elevated in conditional knockouts with no β-CTX difference (Fig. 4D). Histomorphometry confirmed elevated BV/TV, BS/TV, Tb. Th, and Tb. N, along with reduced Tb.Sp and Tb.Pf in osteoblast- and osteoprogenitor-specific knockouts, whereas no significant changes were observed in *Metrnl*$^{Flox/Flox}$*Ctsk*^{Cre} mice (Fig. 4F). Histology showed expanded trabecular bone area, increased Ocn+ OBs, and elevated N.Ob/B.Pm and Ob.S/BS in *Metrnl*$^{Flox/Flox}$*Ocn*^{Cre} and *Metrnl*$^{Flox/Flox}$*Prx1*^{Cre} mice, while osteoclast parameters remained unchanged (Fig. 4E,G). Calcein labeling showed increased MAR and BFR/BS in *Metrnl*$^{Flox/Flox}$*Ocn*^{Cre} and *Metrnl*$^{Flox/Flox}$*Prx1*^{Cre} mice (Fig. 4H,I). Thus, *Metrnl* deletion in osteoblast lineage cells enhances bone formation without affecting osteoclasts, confirming its cell-autonomous role.

3.5 Metrnl Regulates Osteogenic Differentiation Via Intracellular Pathways

As a secreted protein, Metrnl can act through extracellular receptor-mediated mechanisms as well as intracellular pathways. To compare extracellular and intracellular effects of Metrnl, Metrnl knockdown and overexpression MC3T3 cell lines were generated. Overexpression inhibited osteogenic differentiation, while knockdown enhanced mineralization (Fig. 5A,B). To evaluate the exogenous effects of Metrnl, MC3T3 cell lines were directly treated with recombinant Metrnl protein at indicated gradient concentrations (0, 100, 500, and 1000 ng/mL) as shown in (Fig. 5C,D). Notably, intracellular overexpression showed stronger inhibitory effects than recombinant protein treatment, suggesting a dominant intracellular pathway. To rigorously test this, signal peptide-deficient Metrnl overexpression mutants incapable of classical ER-Golgi secretion were constructed (Fig. 5E). ELISA confirmed profoundly diminished secretion from the mutant, while Western blot showed markedly increased intracellular accumulation (Fig. 5F,G). Four MC3T3 groups were compared: signal peptide-deficient Metrnl-OE, wild-type Metrnl-OE, control vector, and vector+rMetrnl (500 ng/mL). Osteogenic induction revealed comparable inhibition between intracellular Metrnl variants, both significantly stronger than extracellular recombinant protein (Fig. 5H,I). These data establish that Metrnl exerts potent intracellular effects and prompted our investigation of its intracellular signaling mechanism.

3.6 Metrnl Interacts With Rack1 During Osteogenic Differentiation

We examined whether intracellular Metrnl functions through protein-protein interactions (Fig. 6A). Using 3×Flag-tagged Metrnl in Co-IP assays followed by silver staining, a prominent band at 35–55 kDa was detected, corresponding to Metrnl-Flag (Fig. 6B). Mass spectrometry identified 30 proteins, among which Rack1 (32 kDa) was detected with multiple unique peptides (Fig. 6C). According to UniProt database, Rack1 is a cytosolic scaffold protein, making it a candidate Metrnl interactor. The interaction between Metrnl and Rack1 was rigorously validated through multiple approaches. First, exogenous Co-IP in HEK293T cells co-transfected with Flag-Metrnl and HA-Rack1 demonstrated that both proteins could reciprocally pull down each other (Fig. 6E). To confirm this interaction under physiological conditions, endogenous Co-IP was performed in BMSCs using anti-Metrnl and anti-Rack1 antibodies. The results confirmed that endogenous Metrnl and Rack1 formed a stable complex in BMSCs (Fig. 6D). Immunofluorescence (IF) staining further revealed that both Metrnl and Rack1 were predominantly localized in the cytoplasm, showing significant spatial co-localization (Fig. 6F). Consistent with these cellular findings, IF analysis of decalcified tibial sections from 12-week-old C57BL/6 mice showed that Metrnl and Rack1 were co-expressed in the nascent trabecular bone region below the growth plate, particularly in cells attached to the trabecular surface (Fig. 6L), confirming the spatial relevance of this interaction *in vivo*. To determine whether the interaction is direct, we performed a GST pull-down assay using recombinant proteins, which confirmed the direct physical binding between Metrnl and Rack1 (Fig. 6K). To further explore the structural basis of this interaction, molecular

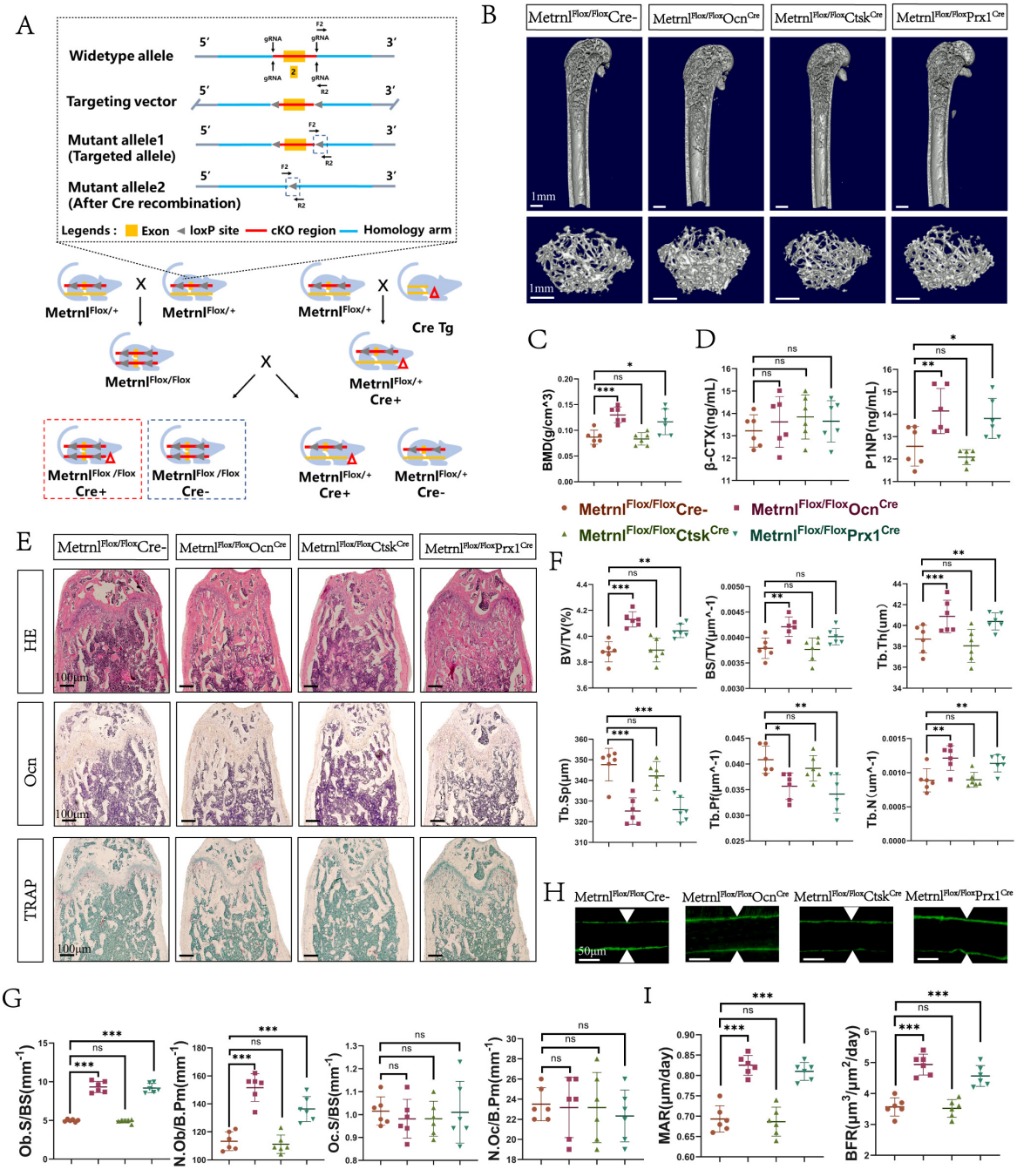

Fig. 4. Effects of osteoblast-specific *Metrnl* deletion on bone mass and cellular differentiation. (A) Schematic of the gene construct and Cre-mediated mating strategy for *Metrnl*$^{Flox/Flox}$ mice. (B) Micro-CT 3D reconstructions showing the distal femur and trabecular bone of *Metrnl*$^{Flox/Flox}$*Cre-*, *Metrnl*$^{Flox/Flox}$ *Ocn*^{Cre} and *Metrnl*$^{Flox/Flox}$ *Prx1*^{Cre}, and *Metrnl*$^{Flox/Flox}$*Ctsk*^{Cre} mice. Scale bar: 1 mm. (C) Bone Mineral Density (BMD) measurement results. (D) ELISA detection of serum bone metabolism markers P1NP and β-CTX. (E) H&E staining, Ocn IHC, and TRAP staining of tibial sections. Scale bar: 100 μm. (F) Bone morphometric parameter analysis, including BV/TV, BS/TV, Tb.Th, Tb. N, Tb.Sp, and Tb. Pf. (G) Histological parameter analysis of osteoblasts and osteoclasts, including Ob.S/BS, N.Ob/B.Pm, Oc.S/BS, and N.Oc/B.Pm. (H) Calcein double labeling experiment showing Mineral Apposition Rate (MAR) and Bone Formation Rate (BFR/BS). Scale bar: 50 μm. (I) Quantitative analysis of Mineral Apposition Rate (MAR) and Bone Formation Rate (BFR/BS). Statistical significance: *$p < 0.05$, **$p < 0.01$, ***$p < 0.001$, "ns" indicates no statistical significance ($p > 0.05$). Error bars represent the mean ± SD, n = 6 per group.

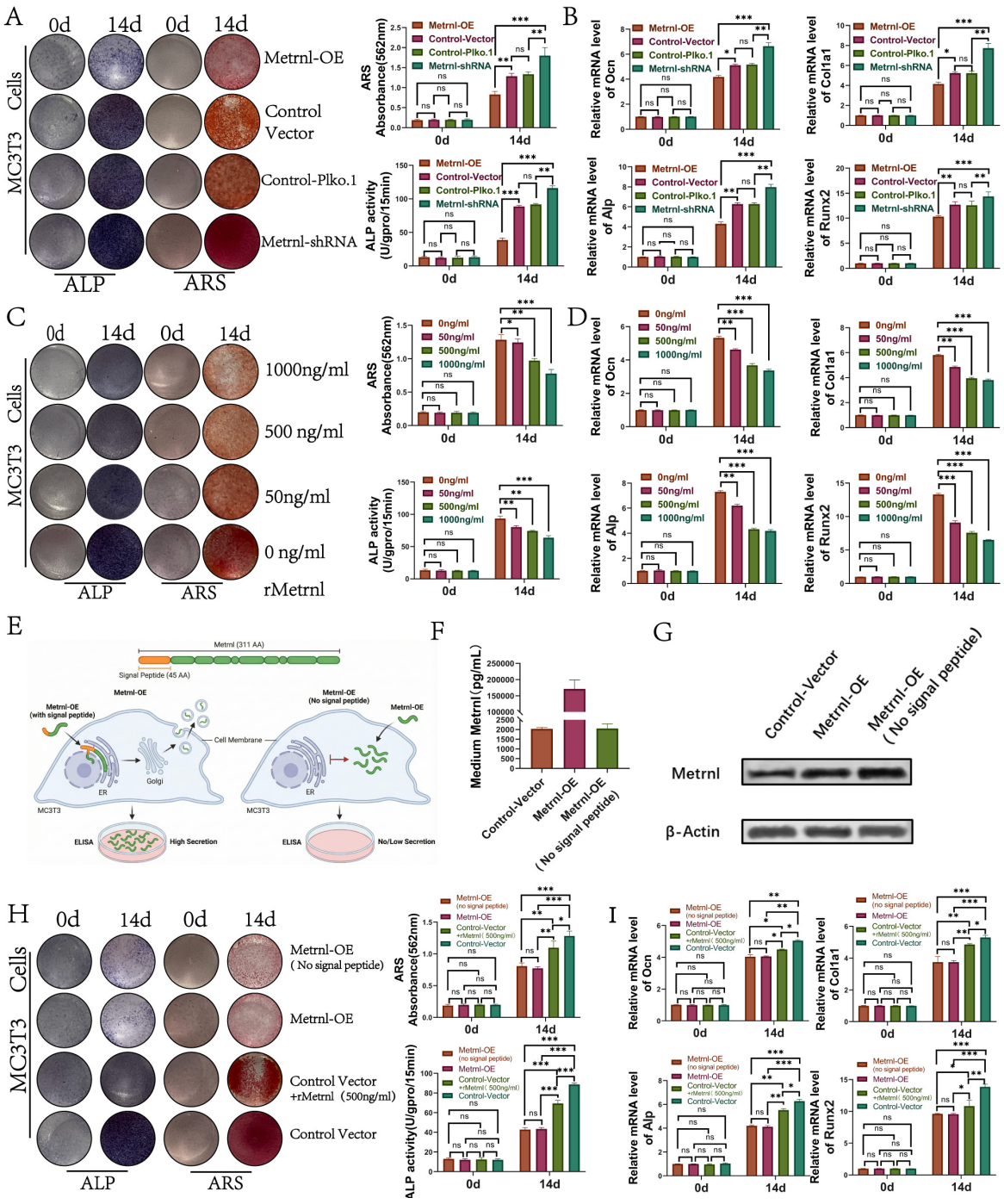

Fig. 5. Investigation of the molecular mechanism of Metrnl in osteogenic differentiation. (A) Effects of Metrnl knockdown and overexpression on osteogenic differentiation in MC3T3 cells, showing ALP and ARS staining. (B) qRT-PCR analysis of osteogenic marker mRNA levels following Metrnl knockdown and overexpression. (C) Effects of various concentrations of recombinant Metrnl protein on MC3T3 osteogenic differentiation (ALP and ARS staining). (D) qRT-PCR analysis of osteogenic marker mRNA levels after treatment with different concentrations of recombinant Metrnl. (E) Schematic of the Metrnl signal peptide function, showing the difference between Metrnl with and without the signal peptide in the secretory pathway. (F) ELISA measurement of Metrnl secretion levels in the culture supernatant of different cell lines. (G) Western blot analysis of intracellular Metrnl expression levels in different cell lines. (H) Osteogenic differentiation of MC3T3 cells under different Metrnl overexpression conditions (ALP and ARS staining). (I) qRT-PCR analysis of osteogenic marker mRNA levels across treatment groups. Data are presented as Mean ± SD; Statistical significance: *$p < 0.05$, **$p < 0.01$, ***$p < 0.001$, "ns" indicates no statistical significance ($p > 0.05$). Error bars represent the mean ± SD.

docking and molecular dynamics (MD) simulations were conducted. The Metrnl-Rack1 complex reached a stable state during a 100 ns simulation, as evidenced by the Root Mean Square Deviation (RMSD) and hydrogen bond analysis (Fig. 6G–I). Structural modeling identified the binding interface, and computational alanine scanning suggested that Ser160 in Rack1 is a critical residue for the interaction, with a predicted binding free energy change ($\Delta\Delta G_{binding}$) of 7.51 kcal/mol upon mutation (Fig. 6J). Collectively, these data demonstrate that Metrnl directly binds to Rack1, potentially forming a functional signaling platform in bone tissue.

3.7 Metrnl Impairs Rack1-PKCα Binding and Suppresses Bmal1 Phosphorylation

Previous studies have shown that Rack1, encoded by Gnb2l1, is a seven WD-repeat scaffold that binds activated PKCα and modulates downstream signaling [36,37,38]. Rack1-PKCα interaction has been reported to stimulate Bmal1 phosphorylation, thereby inhibiting Clock-Bmal1 transcriptional activity and downregulating Cry2 expression [39]. Given previous research demonstrated a negative regulatory role of Cry2 in BMSC osteogenic differentiation, we investigated the effect of Metrnl on this signaling axis [40,41,42]. We first performed a binding pocket analysis using molecular docking and molecular dynamics (MD) simulations. The structural modeling results revealed a significant overlap between the PKCα binding pocket on Rack1 and the Metrnl-Rack1 interaction interface (Fig. 7A). Binding free energy calculations and surface occupancy analysis demonstrated that Metrnl occupies the critical WD-domain pocket of Rack1, which is the essential site for PKCα anchoring (Fig. 7B–D). Specifically, the presence of Metrnl generates significant steric hindrance, effectively obstructing PKCα from accessing its binding site on Rack1. We further employed Western blotting (WB) to examine the expression levels and phosphorylation status of relevant proteins within this signaling pathway. Metrnl overexpression did not alter Rack1 or PKCα protein levels but was associated with reduced Bmal1 phosphorylation and increased Cry2 expression (Fig. 7E), suggesting Metrnl inhibits PKCα-mediated Bmal1 phosphorylation. Co-IP showed that Metrnl overexpression diminished Rack1-PKCα and Bmal1-PKCα interactions (Fig. 7F), consistent with reduced Bmal1 phosphorylation. Immunofluorescence demonstrated that Metrnl overexpression promoted Bmal1 nuclear translocation in BMSCs (Fig. 7G), confirming Metrnl regulates PKCα-Bmal1 signaling.

3.8 Metrnl Promotes Cry2 Transcription Via Rack1 to Inhibit Osteogenesis

qRT-PCR in BMSCs transfected with increasing Metrnl plasmid doses showed dose-dependent Cry2 upregulation. Co-transfection experiments revealed that Rack1 overexpression alone suppressed Cry2, while Metrnl overexpression elevated Cry2. Simultaneous overexpression of both partially reversed the Rack1-mediated suppression of Cry2 (Fig. 7H). Functional assays showed Rack1 overexpression enhanced osteogenic differentiation, whereas Cry2 overexpression suppressed it (Fig. 7I,J). Co-transfection of Metrnl and Rack1 in BMSCs demonstrated that Metrnl's inhibitory effect on osteogenesis was partially rescued by Rack1 co-expression (Fig. 7K,L). These data establish that Metrnl suppresses osteogenesis via Rack1-mediated Cry2 transcription. Tibial sections from 12-week-old *Metrnl*$^{-/-}$ mice showed increased P-Bmal1, decreased Cry2, and elevated Ocn expression (Fig. 7M), validating the pathway *in vivo*.

4. Discussion

This study systematically elucidates Metrnl's expression profile, functional role, and molecular mechanism in bone metabolism, and identifies its clinical association with age-related OP. Proteomic screening identified declined Metrnl levels in elderly osteoporotic women, suggesting a potential association with impaired bone formation during age-related bone loss. This clinical observation provided the foundation for subsequent mechanistic studies. In our clinical cohort, while no significant differences were observed in BMI or serum calcium levels, we noted a marked reduction in 25(OH)D levels among elderly osteoporotic patients. This clinical discrepancy suggests that vitamin D deficiency may be an extrinsic factor influencing the osteogenic microenvironment. Although the present study primarily focused on the intracellular Metrnl-Rack1-PKCα signaling axis, we cannot exclude the possibility that systemic vitamin D status modulates Metrnl expression. Given that Metrnl acts as a bridge between metabolic signals and bone homeostasis, the regulatory crosstalk between Vitamin D and Metrnl warrants further investigation. In our future research, we aim to systematically refine the upstream regulatory mechanisms of Metrnl, specifically focusing on whether vitamin D serves as a key transcriptional or endocrine driver of Metrnl expression in the context of skeletal aging.

In model organisms, Metrnl expression exhibited marked age-dependence: abundant during active bone formation (4–12 weeks) but declining in aged mice (48 weeks) with compromised osteogenic function. This pattern, together with clinical data, supports a negative regulatory role in bone homeostasis. Integration of scRNA-seq and immunohistochemistry precisely localized Metrnl to pro-OBs and mature OBs. Functionally, global *Metrnl* knockout increased trabecular bone mass, trabecular number/thickness, mineralization rate, and biomechanical strength. This phenotype was recapitulated in *Ocn-Cre* and *Prx1-Cre* conditional knockouts, but not in osteoclast-specific knockouts, establishing that Metrnl cell-autonomously inhibits osteogenic differentiation without directly affecting osteoclasts. Mechanistically, we uncovered a dual-mode signaling axis dominated by intracellular action. Metrnl directly

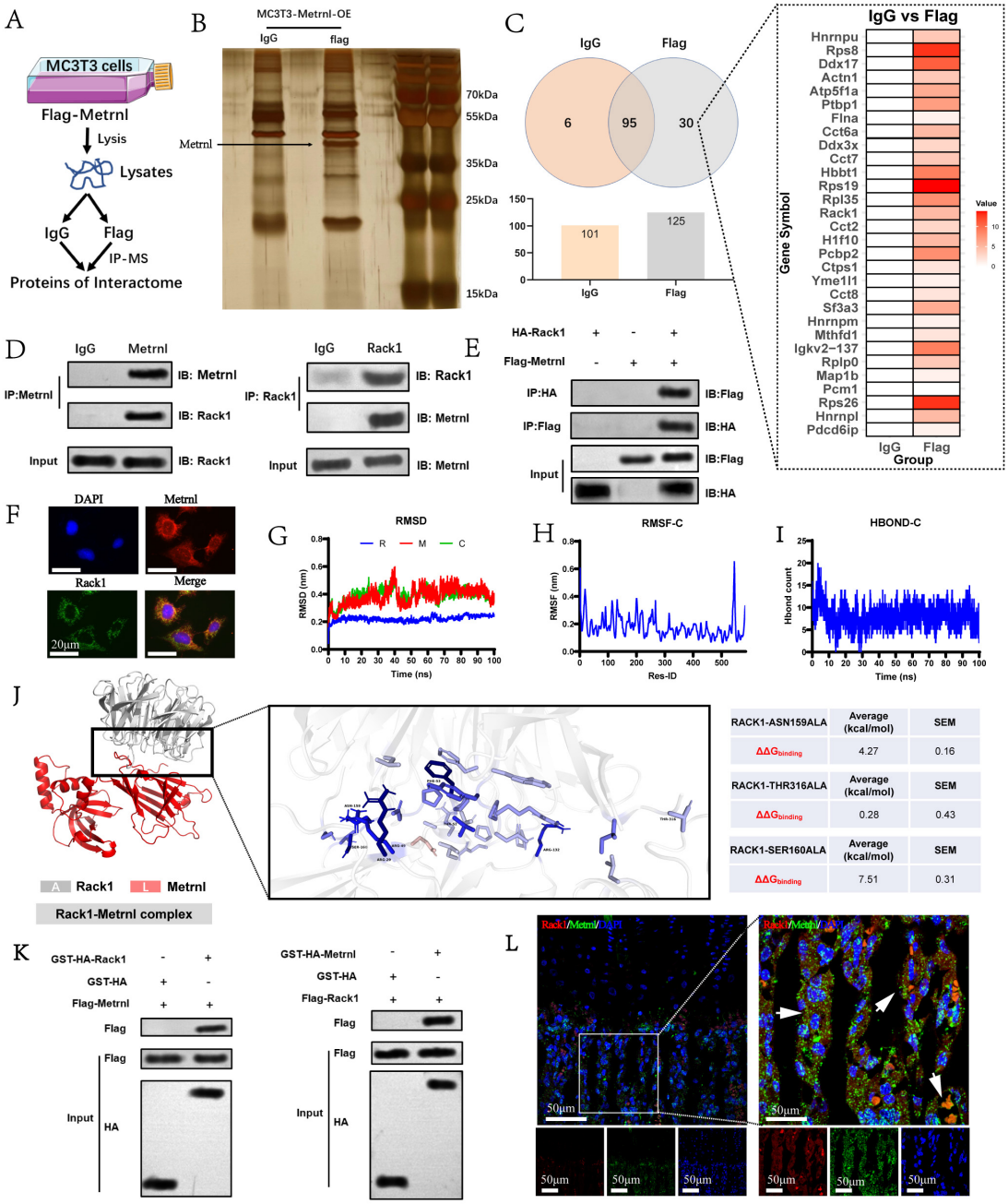

Fig. 6. Interaction between Metrnl and Rack1. (A) Schematic of the experimental workflow for screening Metrnl-interacting proteins using Co-IP and mass spectrometry (MS) in MC3T3-E1 cells. (B) SDS-PAGE silver staining analysis of Flag antibody immunoprecipitates from 3xFlag-Metrnl overexpressing cells. (C) Visualization of mass spectrometry data, including a Venn diagram of specific proteins identified in the Flag group vs. IgG control, and a heatmap of selected candidate proteins. (D) Endogenous Co-IP analysis of Metrnl and Rack1 in bone marrow mesenchymal stem cells (BMSCs). (E) Exogenous Co-IP analysis of Flag-tagged Metrnl and HA-tagged Rack1 in transfected HEK293T cells. (F) Dual immunofluorescence staining of Metrnl (red) and Rack1 (green) in MC3T3-E1 cells; nuclei were counterstained with DAPI (blue). Scale bar: 20 μm. (G–I) Molecular dynamics (MD) simulation parameter analysis over a 100 ns trajectory, including (G) Root Mean Square Deviation (RMSD), (H) Root Mean Square Fluctuation (RMSF), and (I) Hydrogen Bond (HBOND) counts. (J) Structural modeling of the Metrnl-Rack1 docking complex and binding free energy changes (ΔΔGbinding) calculated for specific residue mutations (ASN159ALA, THR316ALA, and SER160ALA). (K) GST pull-down assay using recombinant GST-HA-Metrnl and Flag-Rack1 proteins. (L) Immunofluorescence analysis of Metrnl (green) and Rack1 (red) in decalcified tibial sections of 12-week-old C57BL/6 mice, the white arrows indicate representative co-localization puncta. Scale bar: 50 μm.

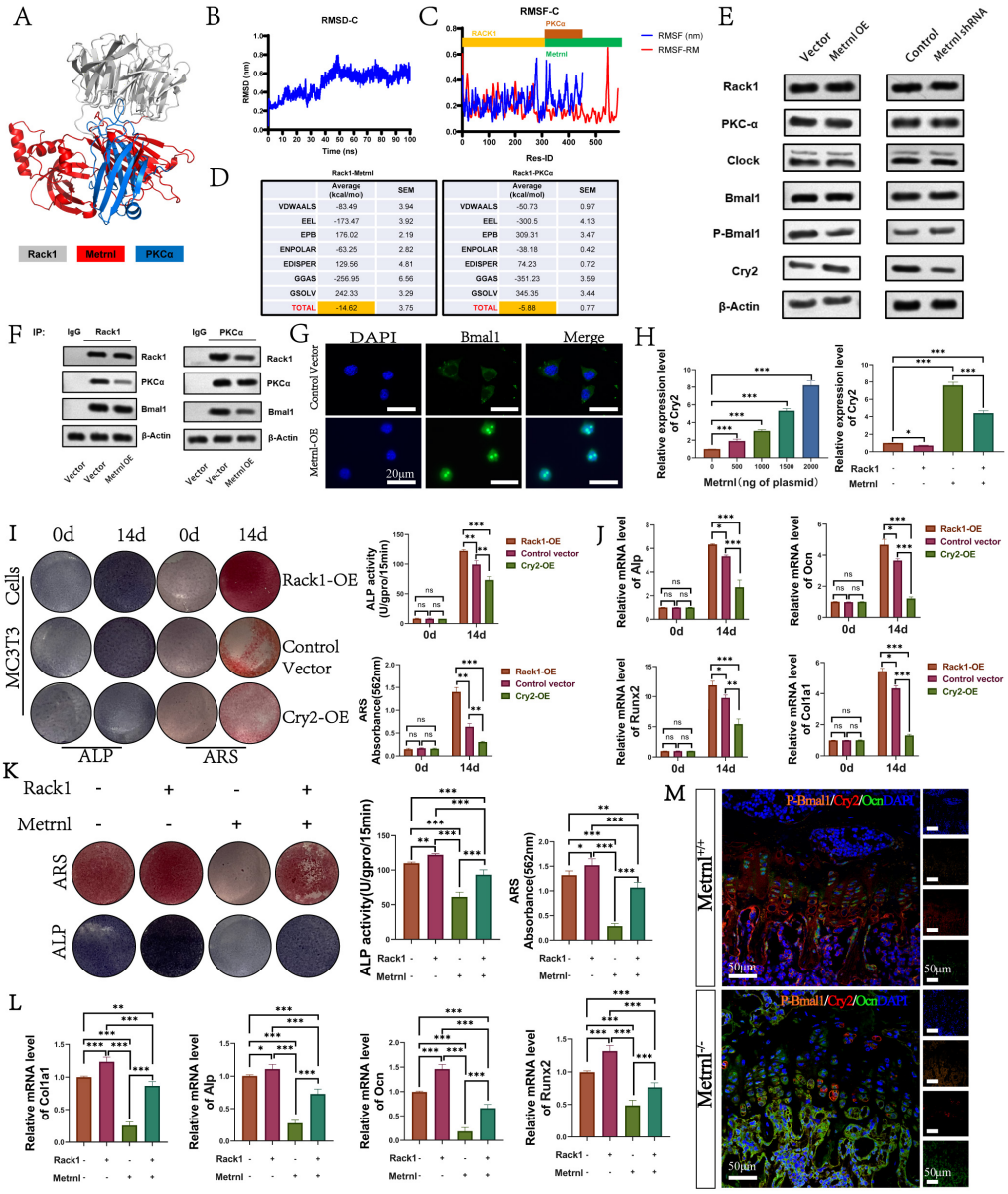

Fig. 7. Metrnl inhibits osteogenic differentiation by regulating the Bmal1/Cry2 axis via a Rack1 competitive binding mechanism. (A) Molecular docking models of Rack1 binding with Metrnl and PKCα. (B) Root Mean Square Deviation (RMSD) curves during 100 ns simulations of Rack1 binding with Metrnl/PKCα. (C) Root Mean Square Fluctuation (RMSF) analysis of key residues. (D) Binding free energy (MM/GBSA) calculations for Rack1 binding with Metrnl/PKCα. (E) Western blot detection of Rack1, PKCα, Clock, Bmal1, P-Bmal1, and Cry2 expression. (F) Co-IP analysis detecting the effects of Metrnl on the assembly of the Rack1/PKCα/Bmal1 complex under different conditions. (G) Immunofluorescence detection of Bmal1 subcellular localization: Observation of the effect of Metrnl overexpression on Bmal1 nuclear translocation in primary BMSCs. Scale bar: 20 μm. (H) qRT-PCR detection of Cry2 mRNA expression following treatment with gradient concentrations of Metrnl and combined Metrnl/Rack1 treatment. (I) Assessment of the effects of Rack1 and Cry2 on osteogenic differentiation phenotypes via ALP staining, ARS staining, and quantitative analysis. (J) qRT-PCR analysis of osteogenic marker mRNA levels across treatment groups. (K) Functional evaluation of Metrnl-Rack1 synergistic regulation of osteogenesis: ALP and ARS staining and quantification in primary BMSCs following single or combined transfection with Metrnl/Rack1 plasmids. (L) Regulation of osteogenic gene expression by Metrnl and Rack1: qRT-PCR detection of osteogenic marker transcription levels in various intervention groups. (M) Multiplex immunofluorescence (TSA) staining for P-Bmal1, Cry2, and Ocn in 12-week-old mouse tibial sections. Scale bar: 50 μm. Statistical significance: *$p < 0.05$, **$p < 0.01$, ***$p < 0.001$, "ns" indicates no statistical significance ($p > 0.05$). Error bars represent the mean ± SD.

binds the scaffold protein Rack1, impairs PKCα-mediated phosphorylation of the Clock-Bmal1 complex, promotes Bmal1 nuclear translocation, enhances Cry2 transcription, and ultimately suppresses osteogenesis.

The spatiotemporal expression pattern of Metrnl has profound physiological implications. Its high expression in juvenile to adult OBs, coinciding with bone accrual, yet declines in aged mice, reflects a finely tuned negative feedback mechanism. We propose that Metrnl may function as a "physiological brake" on bone formation: during rapid bone growth, active osteogenic signals may upregulate Metrnl to prevent excessive bone deposition, while age-related osteoblast attrition reduces Metrnl expression, alleviating its negative regulation. However, this relaxation of feedback appears insufficient to counteract age-related bone loss and may contribute to pathological progression.

Our clinical findings (reduced Metrnl) and genetic results (increased bone mass upon Metrnl deletion) present an apparent biological contradiction that warrants in-depth discussion. Since Metrnl functions as a negative regulator of osteogenesis, its decline in osteoporosis (OP) would theoretically be expected to promote, rather than impair, bone formation. However, we propose that this decline is a passive consequence of "source cell depletion" within the osteogenic niche. Given that Metrnl is precisely localized to pre-osteoblasts and mature osteoblasts, the progressive exhaustion of the osteoblast lineage pool during skeletal aging inevitably leads to a decline in total Metrnl bioavailability. This phenomenon mirrors that of Sclerostin (SOST), a potent Wnt antagonist and established negative regulator of bone formation [43]. Clinical evidence has demonstrated that in states of severe bone loss or extreme aging, serum SOST levels can paradoxically decline—a shift that reflects the depletion of the osteocyte/osteoblast population rather than a pro-anabolic drive [44,45]. Consequently, the reduction of Metrnl in OP likely represents a failed compensatory feedback mechanism: the bone microenvironment attempts to alleviate inhibitory signals by lowering Metrnl levels, yet this "relaxation of the brake" is insufficient to overcome the fundamental impairment in the recruitment and differentiation of osteoprogenitors associated with senescence, which have already undergone a "cliff-like" reduction. This dual-edged nature indicates strict concentration- and context-dependent regulation, requiring precise therapeutic targeting.

Conditional knockout strategies enhanced functional specificity. While global knockout phenotypes are clear, they cannot exclude systemic endocrine effects from other Metrnl-expressing tissues. The recapitulation of phenotypes in Ocn-Cre and Prx1-Cre models, which target mature OBs and early progenitors, respectively, confirms cell-autonomous function in bone. Our findings differ from previous reports suggesting a pro-osteogenic role for Metrnl but are consistent with studies indicating inhibitory effects [32,35]. Discrepancies likely stem from: (1) variable evidence strength—our multi-dimensional approach (global/conditional knockouts, primary cells, tissue validation) versus overexpression or recombinant protein studies; (2) temporal windows—6 weeks (pre-plateau) versus our 12-week (peak bone mass) analysis; and (3) our discovery of the intracellular Rack1-rhythm pathway, which may not be fully engaged by extracellular protein treatment alone. Future studies using inducible knockouts (e.g., Dmp1-CreER) will address stage-specific functions.

A key mechanistic insight from this study is the dual-mode signaling of Metrnl and its coupling to the Clock–Bmal1 system. Regarding the existence forms of Metrnl in bone, our study suggests a dual-localized pattern. Contrary to the conventional view of Metrnl as solely a secreted factor [27,46], our data demonstrate dominant intracellular effects: signal peptide-deficient mutants, though non-secreted, accumulate intracellularly and exhibit wild-type-equivalent osteoinhibitory potency, while extracellular recombinant protein shows limited efficacy. We speculate that Metrnl may exist in a dynamic equilibrium between its nascent, intracellular form (acting as a signaling platform with Rack1) and its secreted form (potentially acting via autocrine/paracrine receptors). The robust intracellular accumulation observed in our Western blots and immunofluorescence suggests that in the bone microenvironment, the non-secreted or pre-secretory pool of Metrnl may be the primary driver of its negative regulatory effects on bone formation. Rack1, a seven-WD-repeat scaffold known for PKC membrane translocation [36], is identified here as a novel Metrnl intracellular effector. Metrnl binding likely impairs Rack1-PKCα interaction via steric hindrance or conformational changes, reducing Bmal1 phosphorylation. Metrnl thus links to the circadian-bone metabolism axis. The Clock-Bmal1 heterodimer, core to the transcriptional-translational feedback loop, is regulated by phosphorylation. Phosphorylated Bmal1 is retained in the cytoplasm, suppressing transcription and downregulating Cry2 [47,48]. Emerging evidence highlights the pivotal role of the circadian clock system in maintaining bone homeostasis [49]. Central clock genes, particularly Bmal1 and Cry2, function as intrinsic molecular oscillators that orchestrate the temporal expression of osteogenic transcription factors [50]. Bmal1 has been identified as a positive regulator of bone mass, with its deficiency leading to impaired osteoblast proliferation and differentiation [51,52]. Conversely, Cry2 acts as a transcriptional repressor in the core clock loop, and its dysregulation is closely associated with age-related bone loss. Cry2 knockout mice exhibit increased bone mass, consistent with our phenotype [42]. Our identification of the Metrnl-Rack1-PKCα-Bmal1-Cry2 axis expands current understanding of the molecular links between circadian regulation and bone metabolism. In summary, our findings position Metrnl as a pivotal metabolic determinant that orchestrates the skeletal response to circadian cues. By fine-tuning the stability of Bmal1 and Cry2 through the Rack1-

PKCα scaffold, Metrnl serves as a molecular link between systemic metabolic status and the local molecular clockwork within the bone microenvironment. Given its age-related decline, Metrnl deficiency may lead to a 'circadian desynchrony' in osteoblasts, rendering bone tissue less responsive to anabolic rhythmicity. Therefore, targeting the Metrnl-mediated circadian interface offers a sophisticated strategy to restore bone homeostasis in age-related osteoporosis.

This study has several limitations, including a relatively small human cohort (n = 10) with a cross-sectional design precluding causality, unknown *in vivo* Metrnl dynamics and half-life-limited spatiotemporal precision (e.g., local gene delivery during fracture healing), an unresolved structural basis of Metrnl-Rack1 interaction, and unexplored effects on broader circadian gene networks. Future studies should validate Metrnl as a bone metabolism biomarker, resolve its structure-function relationship, and develop targeted interventions. Additionally, clinical data in **Supplementary Material 3** reveal a synchronized decline in serum 25(OH)D levels within the elderly OP cohort. While the direct regulatory effect of vitamin D on Metrnl transcription remains to be characterized, this observed correlation suggests a potential 'Vitamin D-Metrnl' axis that warrants further exploration in the context of anabolic recovery in osteoporosis.

From a therapeutic perspective, the timing of Metrnl-targeted interventions is crucial. Given that Metrnl levels are already exhausted in typical senile OP patients due to lineage depletion, further inhibition may yield diminishing returns. Instead, Metrnl inhibitors may be ideally suited for early-stage intervention, such as in perimenopausal women before the "cliff-like" reduction of the osteogenic pool has occurred. By neutralizing this physiological brake while the progenitor reservoir is still relatively intact, it may be possible to maximize bone preservation. Conversely, in conditions characterized by excessive bone formation, such as osteosclerosis or heterotopic ossification, Metrnl or its agonists could be leveraged to therapeutically suppress pathological bone deposition by reinforcing its native negative regulatory axis. Future directions include: (1) screening small-molecule inhibitors of Metrnl-Rack1 interaction; (2) developing bone-targeted delivery systems; (3) exploring synergism with existing OP drugs; and (4) validating efficacy in large animal models. Given Metrnl's pleiotropic roles, skeletal-specific targeting requires rigorous toxicology assessment.

5. Conclusion

This study identifies Metrnl as a negative regulator of bone formation through multi-level functional validation and mechanistic investigation, and characterizes a Metrnl-Rack1-PKCα-Bmal1-Cry2 signaling axis involved in the regulation of bone metabolism. Future studies should evaluate its potential as a biomarker in larger cohorts, elucidate the structural determinants underlying its molecular interactions, and explore targeted therapeutic strategies for bone metabolic diseases.

Abbreviations

Metrnl, Meteorin-like; Rack1, Receptor for activated C kinase 1; PKCα, Protein kinase C alpha; Bmal1, Brain and Muscle ARNT-Like 1; Cry2, Cryptochrome 2; Clock, Circadian Locomotor Output Cycles Kaput; Runx2, Runt-related transcription factor 2; Ocn, Osteocalcin; ALP, Alkaline phosphatase; Col1a1, Collagen type I alpha 1; TRAP, Tartrate-resistant acid phosphatase; OP, Osteoporosis; BMSCs, Bone marrow mesenchymal stem cells; BMMs, Bone marrow–derived macrophages; OBs, Osteoblasts; PDGFRα, Platelet-derived growth factor receptor alpha; Sca-1, Stem cells antigen-1; Prx1, Paired related homeobox 1; Micro-CT, Micro-computed tomography; BMD, Bone mineral density; BV/TV, Bone volume to total volume ratio; BS/TV, Bone surface-to-tissue volume; Tb.N, Trabecular number; Tb.Th, Trabecular thickness; Tb.Sp, Trabecular separation; Tb.Pf, Trabecular pattern factor; MAR, Mineral apposition rate; BFR/BS, Bone formation rate per bone surface; P1NP, Procollagen type 1 N-terminal propeptide; β-CTX, Beta-CrossLaps; TSA, Tyramide signal amplification; ARS, Alizarin Red S; MD, Molecular dynamics; RMSD, Root Mean Square Deviation; RMSF, Root Mean Square Fluctuation; MM/PBSA, Molecular Mechanics Poisson-Boltzmann Surface Area.

Availability of Data and Materials

The datasets utilized and examined in this study can be obtained from the corresponding author upon a reasonable request.

Author Contributions

YH, and YL designed the study, analyzed the data, and revised the paper. WF wrote the paper. WF, KX, MX, TL, X H, WT, CZ, and ZY performed the *in vivo* and *in vitro* experiments. All authors contributed to editorial changes in the manuscript. All authors read and approved the final manuscript. All authors have participated sufficiently in the work and agreed to be accountable for all aspects of the work.

Ethics Approval and Consent to Participate

The animal experiments in this study were reviewed and approved by the Animal Welfare and Ethics Committee of the Department of Laboratory Animal Science, Fudan University (Approval No. 2023-DWYY-22JZS). All procedures involving animals were performed strictly in accordance with the National Standard of China for Institutional Animal Care and Use (GB/T 35892-2018) and relevant international welfare regulations to minimize animal suffering. The study was carried out in accordance with the

ARRIVE guidelines. The ethics for human sample collection were reviewed and approved by the Ethics Committee of the Fifth People's Hospital of Shanghai (Approval No. 2022020). The study was conducted in strict accordance with the ethical guidelines of the Declaration of Helsinki. A written consent was signed by the patients or their families/legal guardians.

Acknowledgment

Our thanks go to the Experimental Center of the Fifth People's Hospital of Shanghai for their provision of experimental instruments and reagents.

Funding

This work was supported by the Shanghai Municipal Health System Key Discipline (New) Program: "2024 Shanghai Municipal Health System Key Discipline - Orthopedic Surgery" (Grant No. 2024ZDXK0033) and Shanghai Science and Technology Innovation Action Plan Natural-Science Foundation Project (Grant No. 23ZR1449800).

Conflicts of Interest

The authors declare no conflicts of interest.

Supplementary Material

Supplementary material associated with this article can be found, in the online version, at https://doi.org/10.31083/FBL53692.

References

[1] Ye C, Ebeling P, Kline G. Osteoporosis. Lancet (London, England). 2025; 406: 2003–2016. https://doi.org/10.1016/S0140-6736(25)01385-6

[2] Leder BZ, Tsai JN, Uihlein AV, Wallace PM, Lee H, Neer RM, et al. Denosumab and teriparatide transitions in postmenopausal osteoporosis (the DATA-Switch study): extension of a randomised controlled trial. Lancet (London, England). 2015; 386: 1147–1155. https://doi.org/10.1016/S0140-6736(15)61120-5

[3] Karsenty G, Khosla S. The crosstalk between bone remodeling and energy metabolism: A translational perspective. Cell Metabolism. 2022; 34: 805–817. https://doi.org/10.1016/j.cmet.2022.04.010

[4] Reid IR, Billington EO. Drug therapy for osteoporosis in older adults. Lancet (London, England). 2022; 399: 1080–1092. https://doi.org/10.1016/S0140-6736(21)02646-5

[5] Yu W, Zhong L, Yao L, Wei Y, Gui T, Li Z, et al. Bone marrow adipogenic lineage precursors promote osteoclastogenesis in bone remodeling and pathologic bone loss. The Journal of Clinical Investigation. 2021; 131: e140214. https://doi.org/10.1172/JCI140214

[6] Chang LL, Eastell R, Miller PD. Continuation of Bisphosphonate Therapy for Osteoporosis beyond 5 Years. The New England Journal of Medicine. 2022; 386: 1467–1469. https://doi.org/10.1056/NEJMclde2115900

[7] Ma S, Goh EL, Jin A, Bhattacharya R, Boughton OR, Patel B, et al. Long-term effects of bisphosphonate therapy: perforations, microcracks and mechanical properties. Scientific Reports. 2017; 7: 43399. https://doi.org/10.1038/srep43399

[8] Billington E, Aghajafari F, Skulsky E, Kline GA. Bisphosphonates. BMJ (Clinical Research Ed.). 2024; 386: e076898. https://doi.org/10.1136/bmj-2023-076898

[9] Mizoguchi T, Ono N. The diverse origin of bone-forming osteoblasts. Journal of Bone and Mineral Research : the Official Journal of the American Society for Bone and Mineral Research. 2021; 36: 1432–1447. https://doi.org/10.1002/jbmr.4410

[10] Amarasekara DS, Kim S, Rho J. Regulation of Osteoblast Differentiation by Cytokine Networks. International Journal of Molecular Sciences. 2021; 22: 2851. https://doi.org/10.3390/ijms22062851

[11] Dalle Carbonare L, Bertacco J, Marchetto G, Cheri S, Deiana M, Minoia A, et al. Methylsulfonylmethane enhances MSC chondrogenic commitment and promotes pre-osteoblasts formation. Stem Cell Research & Therapy. 2021; 12: 326. https://doi.org/10.1186/s13287-021-02396-5

[12] Chen E, Liu G, Zhou X, Zhang W, Wang C, Hu D, et al. Concentration-dependent, dual roles of IL-10 in the osteogenesis of human BMSCs via P38/MAPK and NF-κB signaling pathways. FASEB Journal : Official Publication of the Federation of American Societies for Experimental Biology. 2018; 32: 4917–4929. https://doi.org/10.1096/fj.201701256RRR

[13] Han Y, Gao H, Gan X, Liu J, Bao C, He C. Roles of IL-11 in the regulation of bone metabolism. Frontiers in Endocrinology. 2023; 14: 1290130. https://doi.org/10.3389/fendo.2023.1290130

[14] Li S, Liu G, Hu S. Osteoporosis: interferon-gamma-mediated bone remodeling in osteoimmunology. Frontiers in Immunology. 2024; 15: 1396122. https://doi.org/10.3389/fimmu.2024.1396122

[15] Kim BJ, Koh JM. Coupling factors involved in preserving bone balance. Cellular and Molecular Life Sciences : CMLS. 2019; 76: 1243–1253. https://doi.org/10.1007/s00018-018-2981-y

[16] Sims NA, Lévesque JP. Oncostatin M: Dual Regulator of the Skeletal and Hematopoietic Systems. Current Osteoporosis Reports. 2024; 22: 80–95. https://doi.org/10.1007/s11914-023-00837-z

[17] Yao Q, He L, Bao C, Yan X, Ao J. The role of TNF-α in osteoporosis, bone repair and inflammatory bone diseases: A review. Tissue and Cell. 2024; 89: 102422. https://doi.org/10.1016/j.tice.2024.102422

[18] Constanze B, Popper B, Aggarwal BB, Shakibaei M. Evidence that TNF-β suppresses osteoblast differentiation of mesenchymal stem cells and resveratrol reverses it through modulation of NF-κB, Sirt1 and Runx2. Cell and Tissue Research. 2020; 381: 83–98. https://doi.org/10.1007/s00441-020-03188-8

[19] Ura K, Morimoto I, Watanabe K, Saito K, Yanagihara N, Eto S. Interleukin (IL)-4 and IL-13 inhibit the differentiation of murine osteoblastic MC3T3-E1 cells. Endocrine Journal. 2000; 47: 293–302. https://doi.org/10.1507/endocrj.47.293

[20] Razawy W, Alves CH, Koedam M, Asmawidjaja PS, Mus AMC, Oukka M, et al. IL-23 receptor deficiency results in lower bone mass via indirect regulation of bone formation. Scientific Reports. 2021; 11: 10244. https://doi.org/10.1038/s41598-021-89625-2

[21] Loh HY, Norman BP, Lai KS, Cheng WH, Nik Abd Rahman NMA, Mohamed Alitheen NB, et al. Post-Transcriptional Regulatory Crosstalk between MicroRNAs and Canonical TGF-β/BMP Signalling Cascades on Osteoblast Lineage: A Comprehensive Review. International Journal of Molecular Sciences. 2023; 24: 6423. https://doi.org/10.3390/ijms24076423

[22] Wu M, Wu S, Chen W, Li YP. The roles and regulatory mechanisms of TGF-β and BMP signaling in bone and cartilage development, homeostasis and disease. Cell Research. 2024; 34: 101–123. https://doi.org/10.1038/s41422-023-00918-9

[23] Li ZY, Zheng SL, Wang P, Xu TY, Guan YF, Zhang YJ, et al. Subfatin is a novel adipokine and unlike Meteorin in adipose and brain expression. CNS Neuroscience & Therapeutics. 2014; 20: 344–354. https://doi.org/10.1111/cns.12219

[24] Jørgensen JR, Fransson A, Fjord-Larsen L, Thompson LH,

Houchins JP, Andrade N, et al. Cometin is a novel neurotrophic factor that promotes neurite outgrowth and neuroblast migration in vitro and supports survival of spiral ganglion neurons in vivo. Experimental Neurology. 2012; 233: 172–181. https://doi.org/10.1016/j.expneurol.2011.09.027

[25] Li ZY, Fan MB, Zhang SL, Qu Y, Zheng SL, Song J, et al. Intestinal Metrnl released into the gut lumen acts as a local regulator for gut antimicrobial peptides. Acta Pharmacologica Sinica. 2016; 37: 1458–1466. https://doi.org/10.1038/aps.2016.70

[26] Bridgewood C, Russell T, Weedon H, Baboolal T, Watad A, Sharif K, et al. The novel cytokine Metrnl/IL-41 is elevated in Psoriatic Arthritis synovium and inducible from both entheseal and synovial fibroblasts. Clinical Immunology (Orlando, Fla.). 2019; 208: 108253. https://doi.org/10.1016/j.clim.2019.108253

[27] Miao ZW, Chen J, Chen CX, Zheng SL, Zhao HY, Miao CY. Metrnl as a secreted protein: Discovery and cardiovascular research. Pharmacology & Therapeutics. 2024; 263: 108730. https://doi.org/10.1016/j.pharmthera.2024.108730

[28] Zheng SL, Li ZY, Song J, Liu JM, Miao CY. Metrnl: a secreted protein with new emerging functions. Acta Pharmacologica Sinica. 2016; 37: 571–579. https://doi.org/10.1038/aps.2016.9

[29] Li ZY, Song J, Zheng SL, Fan MB, Guan YF, Qu Y, et al. Adipocyte Metrnl Antagonizes Insulin Resistance Through PPARγ Signaling. Diabetes. 2015; 64: 4011–4022. https://doi.org/10.2337/db15-0274

[30] Lee JO, Byun WS, Kang MJ, Han JA, Moon J, Shin MJ, et al. The myokine meteorin-like (metrnl) improves glucose tolerance in both skeletal muscle cells and mice by targeting AMPKα2. The FEBS Journal. 2020; 287: 2087–2104. https://doi.org/10.1111/febs.15301

[31] Reboll MR, Klede S, Taft MH, Cai CL, Field LJ, Lavine KJ, et al. Meteorin-like promotes heart repair through endothelial KIT receptor tyrosine kinase. Science (New York, N.Y.). 2022; 376: 1343–1347. https://doi.org/10.1126/science.abn3027

[32] Gong W, Liu Y, Wu Z, Wang S, Qiu G, Lin S. Meteorin-Like Shows Unique Expression Pattern in Bone and Its Overexpression Inhibits Osteoblast Differentiation. PloS One. 2016; 11: e0164446. https://doi.org/10.1371/journal.pone.0164446

[33] Invernizzi M, de Sire A, Carda S, Venetis K, Renò F, Cisari C, et al. Bone Muscle Crosstalk in Spinal Cord Injuries: Pathophysiology and Implications for Patients' Quality of Life. Current Osteoporosis Reports. 2020; 18: 422–431. https://doi.org/10.1007/s11914-020-00601-7

[34] Gonzalez-Gil AM, Elizondo-Montemayor L. The Role of Exercise in the Interplay between Myokines, Hepatokines, Osteokines, Adipokines, and Modulation of Inflammation for Energy Substrate Redistribution and Fat Mass Loss: A Review. Nutrients. 2020; 12: 1899. https://doi.org/10.3390/nu12061899

[35] Huang R, Balu AR, Molitoris KH, White JP, Robling AG, Ayturk UM, et al. The role of Meteorin-like in skeletal development and bone fracture healing. Journal of Orthopaedic Research : Official Publication of the Orthopaedic Research Society. 2022; 40: 2510–2521. https://doi.org/10.1002/jor.25286

[36] Steinberg SF. Structural basis of protein kinase C isoform function. Physiological Reviews. 2008; 88: 1341–1378. https://doi.org/10.1152/physrev.00034.2007

[37] Battaini F, Pascale A. Protein kinase C signal transduction regulation in physiological and pathological aging. Annals of the New York Academy of Sciences. 2005; 1057: 177–192. https://doi.org/10.1196/annals.1356.011

[38] Racaud-Sultan C, Vergnolle N. GSK3β, a Master Kinase in the Regulation of Adult Stem Cell Behavior. Cells. 2021; 10: 225. https://doi.org/10.3390/cells10020225

[39] Robles MS, Boyault C, Knutti D, Padmanabhan K, Weitz CJ. Identification of RACK1 and protein kinase Calpha as integral components of the mammalian circadian clock. Science (New York, N.Y.). 2010; 327: 463–466. https://doi.org/10.1126/science.1180067

[40] Tang Z, Xu T, Li Y, Fei W, Yang G, Hong Y. Inhibition of CRY2 by STAT3/miRNA-7-5p Promotes Osteoblast Differentiation through Upregulation of CLOCK/BMAL1/P300 Expression. Molecular Therapy. Nucleic Acids. 2020; 19: 865–876. https://doi.org/10.1016/j.omtn.2019.12.020

[41] Tsang K, Liu H, Yang Y, Charles JF, Ermann J. Defective circadian control in mesenchymal cells reduces adult bone mass in mice by promoting osteoclast function. Bone. 2019; 121: 172–180. https://doi.org/10.1016/j.bone.2019.01.016

[42] Maronde E, Schilling AF, Seitz S, Schinke T, Schmutz I, van der Horst G, et al. The clock genes Period 2 and Cryptochrome 2 differentially balance bone formation. PloS One. 2010; 5: e11527. https://doi.org/10.1371/journal.pone.0011527

[43] Marini F, Giusti F, Palmini G, Brandi ML. Role of Wnt signaling and sclerostin in bone and as therapeutic targets in skeletal disorders. Osteoporosis International : a Journal Established as Result of Cooperation between the European Foundation for Osteoporosis and the National Osteoporosis Foundation of the USA. 2023; 34: 213–238. https://doi.org/10.1007/s00198-022-06523-7

[44] Kocijan R, Muschitz C, Fahrleitner-Pammer A, Amrein K, Pietschmann P, Haschka J, et al. Serum sclerostin levels are decreased in adult patients with different types of osteogenesis imperfecta. The Journal of Clinical Endocrinology and Metabolism. 2014; 99: E311–9. https://doi.org/10.1210/jc.2013-2244

[45] Reppe S, Noer A, Grimholt RM, Halldórsson BV, Medina-Gomez C, Gautvik VT, et al. Methylation of bone SOST, its mRNA, and serum sclerostin levels correlate strongly with fracture risk in postmenopausal women. Journal of Bone and Mineral Research : the Official Journal of the American Society for Bone and Mineral Research. 2015; 30: 249–256. https://doi.org/10.1002/jbmr.2342

[46] Li J, Ye P, Si J, Xiang G. Meteorin-like/Metrnl: A pleiotropic cytokine implicated in metabolic, inflammatory and malignant disorders. Cytokine & Growth Factor Reviews. 2026; 87: 64–72. https://doi.org/10.1016/j.cytogfr.2025.12.003

[47] Tamaru T, Hattori M, Honda K, Nakahata Y, Sassone-Corsi P, van der Horst GTJ, et al. CRY Drives Cyclic CK2-Mediated BMAL1 Phosphorylation to Control the Mammalian Circadian Clock. PLoS Biology. 2015; 13: e1002293. https://doi.org/10.1371/journal.pbio.1002293

[48] Yuan VG. Rhythms in Remodeling: Posttranslational Regulation of Bone by the Circadian Clock. Biomedicines. 2025; 13: 705. https://doi.org/10.3390/biomedicines13030705

[49] Qin Y, Chen ZH, Wu JJ, Zhang ZY, Yuan ZD, Guo DY, et al. Circadian clock genes as promising therapeutic targets for bone loss. Biomedicine & Pharmacotherapy = Biomedecine & Pharmacotherapie. 2023; 157: 114019. https://doi.org/10.1016/j.biopha.2022.114019

[50] Luo B, Zhou X, Tang Q, Yin Y, Feng G, Li S, et al. Circadian rhythms affect bone reconstruction by regulating bone energy metabolism. Journal of Translational Medicine. 2021; 19: 410. https://doi.org/10.1186/s12967-021-03068-x

[51] Ze Y, Wu Y, Tan Z, Li R, Li R, Gao W, et al. Signaling pathway mechanisms of circadian clock gene Bmal1 regulating bone and cartilage metabolism: a review. Bone Research. 2025; 13: 19. https://doi.org/10.1038/s41413-025-00403-6

[52] Yu S, Tang Q, Chen G, Lu X, Yin Y, Xie M, et al. Circadian rhythm modulates endochondral bone formation via MTR1/AMPKβ1/BMAL1 signaling axis. Cell Death and Differentiation. 2022; 29: 874–887. https://doi.org/10.1038/s41418-021-00919-4